Geology, U-Pb geochronology and stable isotope geochemistry of the Heihaibei gold deposit in the southern part of the Eastern Kunlun Orogenic Belt, China : A granitic intrusion-related gold deposit?

Yu, Lu

2022-05

Yu , L , Sun , F , Beier , C , Wu , D , Li , L , Wang , L , Huang , G , Fan , X & Xu , C 2022 , ' Geology, U-Pb geochronology and stable isotope geochemistry of the Heihaibei gold deposit in the southern part of the Eastern Kunlun Orogenic Belt, China : A granitic intrusion-related gold deposit? ' , Ore Geology Reviews , vol. 144 , 104859 . https://doi.org/10.1016/j.oregeorev.2022.104859

http://hdl.handle.net/10138/343448
https://doi.org/10.1016/j.oregeorev.2022.104859

Ore Geology Reviews 144 (2022) 104859

Contents lists available at ScienceDirect

Ore Geology Reviews

journal homepage: www.elsevier.com/locate/oregeorev

Geology, U-Pb geochronology and stable isotope geochemistry of the Heihaibei gold deposit in the southern part of the Eastern Kunlun Orogenic Belt, China: A granitic intrusion-related gold deposit?

Lu Yu [a,*], Fengyue Sun [a,*], Christoph Beier [b], Dongqian Wu [a], Liang Li [c], Li Wang [a], Guobiao Huang [d], Xingzhu Fan [a], Chenghan Xu [a]

[a] College of Earth Sciences, Jilin University, Changchun 130061, China
[b] Department of Geosciences and Geography, Research Programme of Geology and Geophysics (GeoHel), University of Helsinki, Helsinki 00014, Finland
[c] School of Resource Environment and Earth Science, Yunnan University, Kunming 650500, China
[d] Bureau of Geological Exploration & Development of Qinghai Province, Xining 810008, China

ARTICLE INFO

Keywords:
Intrusion-related gold deposit
Monzogranites
Zircon U-Pb dating
LA-ICP-MS trace element analysis
H-O-S-Pb-Hf isotopes
Eastern Kunlun Orogenic Belt

ABSTRACT

The Heihaibei gold deposit is a newly discovered gold deposit in the southern part of the Eastern Kunlun Orogenic Belt. Its most distinctive features are that the gold mineralization is hosted in monzogranite, and that the presence of pre-ore (possibly *syn*-ore) monzogranite and post-ore gabbro allows to constrain the mineralization's formation age. Zircons from the monzogranites yield U-Pb ages of 454 ± 3 Ma, while zircons separated from the gabbro dikes cutting the monzogranites and gold mineralized body yield U-Pb ages of 439 ± 3 Ma, which is interpreted to be the minimum age of the Au mineralizing event. Combined with the regional geological background, we proposed that the Heihaibei Au mineralization occurred during the subduction stage of the Early Paleozoic Proto-Tethys ocean.

The ore assemblage is dominated by pyrite, arsenopyrite and native gold. The hydrothermal alteration that has led to the peculiar enrichment of Au is not systematically distributed and displays no clear concentric zoning pattern. The main mineralization formed during three stages: the K-feldspar-quartz-pyrite (Py1)-arsenopyrite-sericite-epidote stage (I), the quartz-pyrite (Py2)-native gold-chlorite stage (II), and the quartz-carbonate stage (III). The main gold mineralization occurred during stage II. Fluid inclusion homogenization temperature and salinities decrease from stage I (Th., 268–412 °C; W., 6.87–16.63 wt% NaCl equiv.) to stage II (Th., 183–288 °C; W., 3.69–14.84 wt% NaCl equiv.). The $\delta^{18}O$ and δD values ($\delta^{18}O_{H2O}$ = 4.9 to 9.7‰; $\delta D_{V\text{-}SMOW}$ = -84.1‰ to −81.1‰) of quartz samples from stage I and stage II are comparable to a magmatic-hydrothermal ore-forming fluid that possibly underwent fluid-rock interaction with the Nachitai Group metamorphic rocks during the early ore-forming stage. The relatively uniform $\delta^{34}S$ values ($\delta^{34}S_{V\text{-}CDT}$ = 7.7 to 8.5‰) are slightly elevated compared to magmatic $\delta^{34}S$ values, but could be derived from a magma if a significant crustal melt component is present. Moreover, the $\delta^{34}S$ values are within the S isotopic composition range of a granitic reservoir, suggesting that they are probably inherited from the Heihaibei monzogranites. The Pb and Hf isotope compositions imply a close genetic association between the gold mineralization and granitic magmatism, which are both the products of the mixing of crustal and mantle sources. The trace element compositions of pyrite provide additional evidence that the gold mineralization in the Heihaibei deposit was related to the magmatism. Compared with the typical characteristics of orogenic gold and intrusion-related gold systems (IRGS) deposits, the Heihaibei gold deposit may instead be classified as a granitic intrusion-related gold deposit.

1. Introduction

A number of gold deposits/fields, such as the Wulonggou (>70 t Au; Zhang and Sun, 2018) and Gouli (>110 t Au; Chen et al., 2020) goldfields, the Dachang (220 t; Feng and Zhang, 2002), Kendekeke, and Tuolugou gold deposits (Feng, et al., 2002; Zhao et al., 2006; Feng et al.,

* Corresponding authorsat: College of Earth Sciences, Jilin University, No. 2199 Jianshe Street, Changchun 130061, PR China.
E-mail addresses: yulujlu@hotmail.com (L. Yu), fengyuesun63@outlook.com (F. Sun).

https://doi.org/10.1016/j.oregeorev.2022.104859
Received 8 January 2021; Received in revised form 23 March 2022; Accepted 23 March 2022
Available online 26 March 2022

Table 1
Typical gold deposits in the EKOB.

Deposit	Resources (t)	Genetic type	Mineralization age (Ma)	Mineral and method	References
Guoluolongwa	40.00	Orogenic type	375 ± 11; 354 ± 7; 202.7 ± 1.5	Pyrite, Re-Os; Sericite, Ar-Ar	(Chen et al., 2020; Xiao et al., 2014)
Annage		Orogenic type	383 ± 6	Pyrite, Re-Os	(Chen et al., 2020)
Shuizhadonggou	45.00	Orogenic type	230.8 ± 1.7	Sericite, Ar-Ar	(Zhang et al., 2017)
Dachang	220.00	Orogenic type	218.6 ± 3.2	Sericite, Ar-Ar	(Feng et al., 2002)
Tuolugou	4.00	Hydrothermal-exhalation sedimentary type	429 ± 29	Pyrite, Re-Os	(Feng et al., 2009)
Kendekeke		Skarn type	207.8 ± 1.9	Plagioclase, Ar-Ar	(Zhao et al., 2006)

2009), have been discovered in the East Kunlun Orogenic Belt (EKOB) in the last two decades. The mineralization ages display two peaks (Late Paleozoic and Triassic), and, integrated into the geological background, imply that they were mainly formed in a collisional or post-collisional regime related to the closure of the Proto-Tethys and Paleo-Tethys Oceans, respectively (Table 1; Chen et al., 2020). Most of them exhibit quartz vein type or fracture-hosted pervasive alteration type mineralizations and are spatially controlled by brittle-ductile shear zones and, thus have been classified as orogenic gold deposits (Feng, 2002; Zhao, 2004). However, orogenic gold deposits (Groves et al., 1998) also share common characteristics with intrusion-related gold deposits or systems (IRGD, IRGS) (Sillitoe 1991; Goldfarb and Groves 2015), which has led to confusion in distinguishing the two types of deposits.

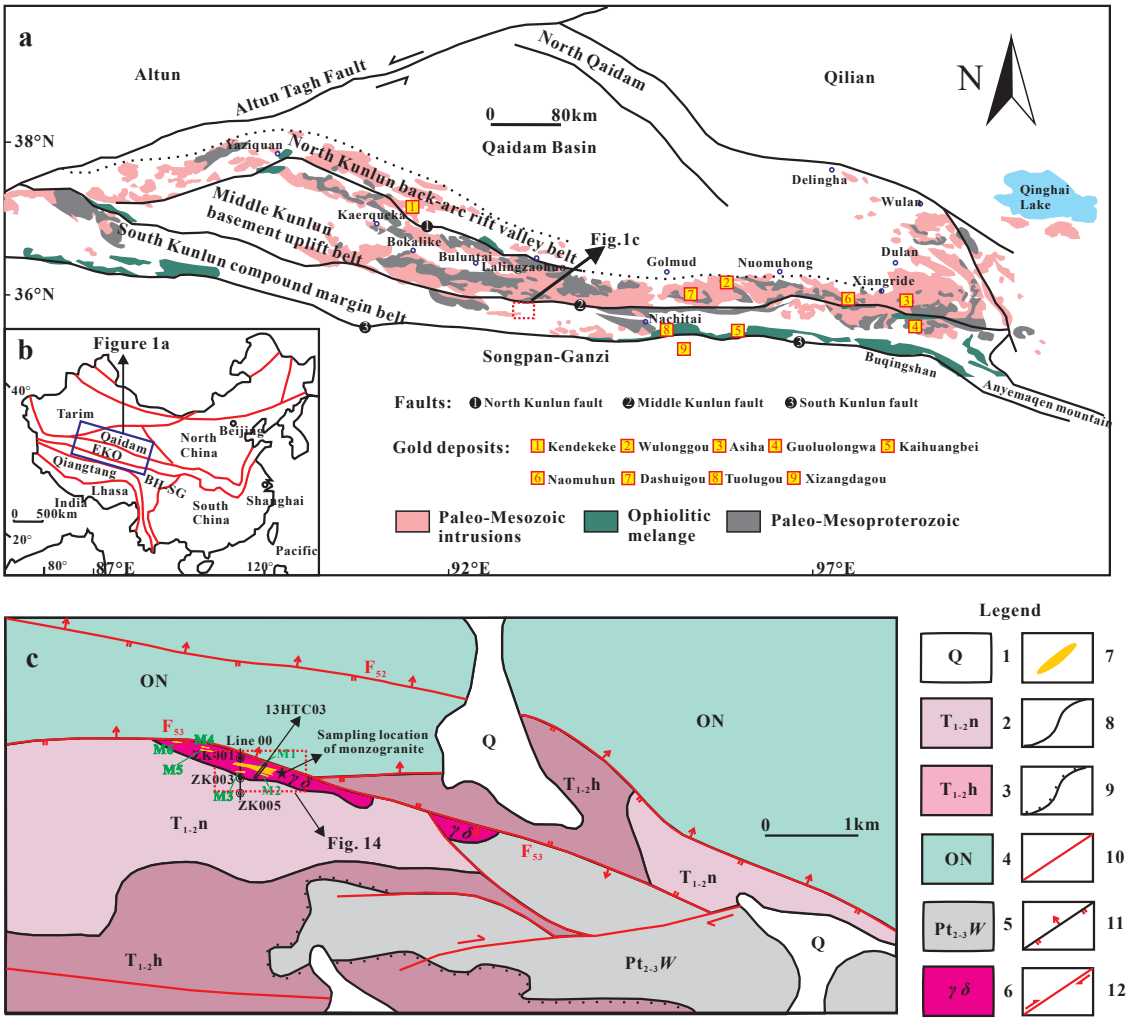

1. Quaternary; 2. Lower-Middle Triassic Naocangjiangou Formation; 3. Lower-Middle Triassic Hongshuichuan Formation; 4. Ordovician Nachitai Group; 5. Meso-Neoproterozoic Wanbaogou Group; 6. Monzogranite; 7. Gold ore bodies; 8. Geological boundary; 9. Angular unconformity 10. Fault; 11. Reverse fault; 12. Parallel displacement fault;

Fig. 1. (a) Geological map showing the regional structures of the EKOB (after He et al. 2018); (b) Schematic map showing the position of the EKOB; (c) Geological map of the Heihaibei gold deposit (based on the 1:10000 geological map of Heihaibei gold deposit, Bureau of Geological Exploration & Development of Qinghai Province).

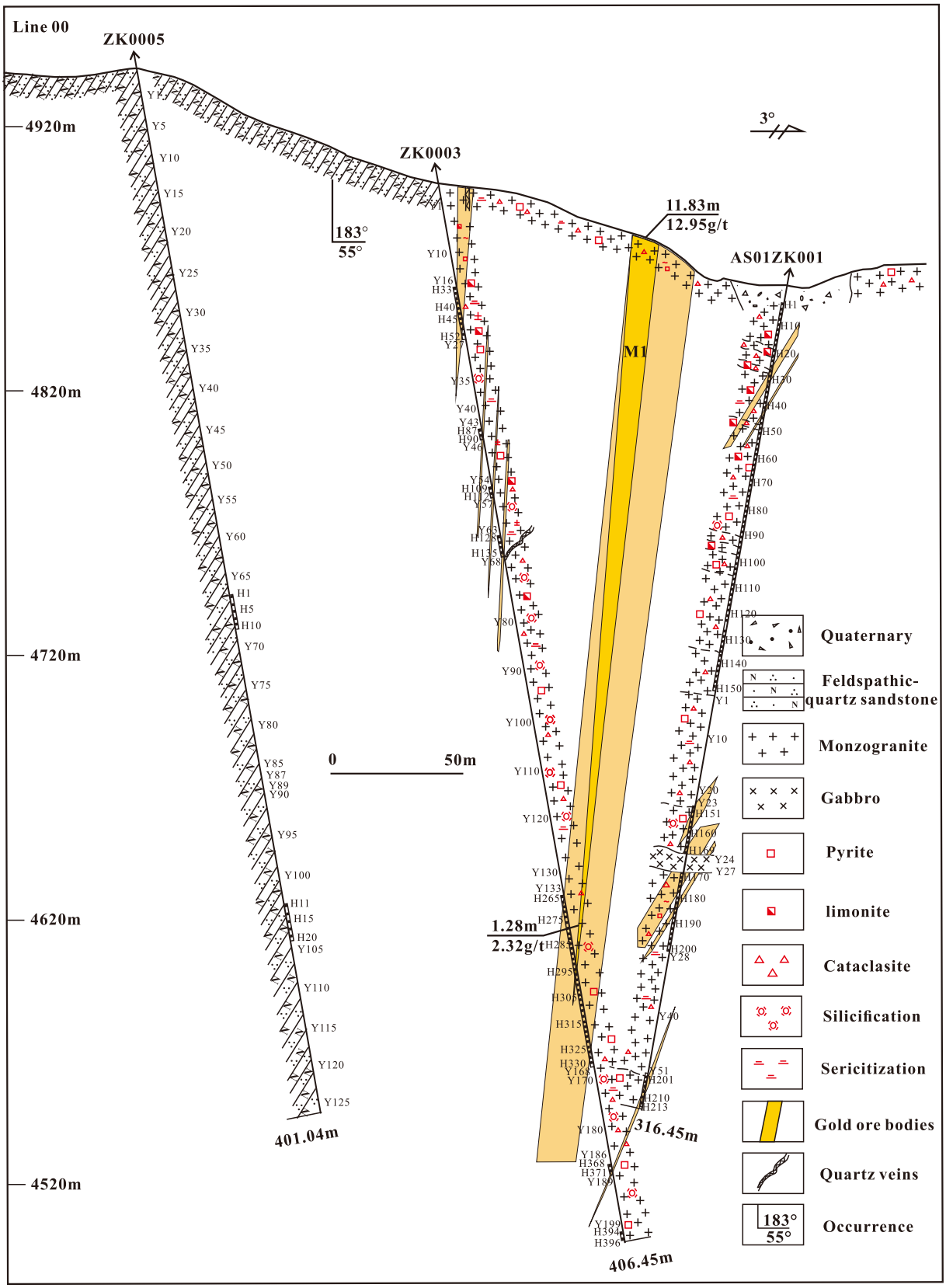

Fig. 2. Line 00 drillings profile map showing the occurrence and morphology of major gold ore bodies in the Heihaibei gold deposit.

Orogenic gold deposits are generally formed from fluids and metals that exsolve from coeval intrusive magmas or by metamorphic devolatilisation of volcanic-sedimentary rocks (Goldfarb et al., 2001; Groves et al., 2020; Patten et al., 2020). IRGDs also form by ore-forming fluids similar to orogenic gold deposits, but differ in that they are composed of several styles of hydrothermal mineralization that are genetically related to the emplacement and cooling of granitic plutons (Hart et al., 2004; Mernagh et al., 2007). Some gold deposits in the EKOB have genetically been linked to granitic magmatism, such as the Naomuhun, Dashuigou and Xizangdagou gold deposits (Li et al., 2017). Among them, Ar-Ar ages (227.84 ± 1.13 Ma) of sericite from the Naomuhun gold deposit are coeval (±8 m.y.) with zircon U-Pb ages (235.8 ± 0.8 Ma) from the associated granitic plutons (Li et al., 2017). From a more regional perspective, a number of IRGDs have also been reported in the adjacent western Qinling area (Sui et al., 2017).

The Heihaibei gold deposit is located at the southern part of the EKOB. The most distinctive features of this deposit are that the gold mineralization is hosted in monzogranites, and that the presence of pre-ore (possibly *syn*-ore) monzogranite and post-ore gabbro allow us to constrain the age of the gold mineralization. In addition, soil anomaly characteristics show that Au, W and Sb anomalies exist around the monzogranites, while Pb and Zn anomalies occur in the northern part 1–2 km away (Huang, 2018), which indicate a possible genetic link between the gold mineralization and monzogranites.

Here, we present new zircon U-Pb ages on the pre-ore (possibly *syn*-ore) monzogranite and post-ore gabbro to constrain the gold mineralization age, and combined with the regional geological background, the subduction related tectonic setting responsible for the Heihaibei gold deposit is discussed. We then use fluid inclusions micro-thermometric results, stable isotope data, as well as trace element compositions of pyrite from the Heihaibei gold deposit to investigate the sources of the ore-forming fluids and materials. Finally, compared with the typical characteristics of orogenic gold deposits and IRGS deposits, we conclude that the Heihaibei gold deposit may instead be classified as a granitic intrusion-related gold deposit.

2. Regional geology

The EKOB is part of the Tibetan Plateau, NW China and is situated close to the Qaidam block (QDM) in the north and the Bayan Har-Songpanganzi Terrane (BH-SG) in the south. The belt extends for ~1500 km from east to west and has a width of 50–200 km along the northern margin of the Tibetan Plateau (Fig. 1b). From north to south, the EKOB can be divided into three sub-parallel EW-striking belts, the North Eastern Kunlun Caledonian back-arc basin belt (NKB), the Central Eastern Kunlun basement uplifted and granitic belt (CKB), and the South Eastern Kunlun composite accretion belt (SKB; Fig. 1a), bordered by the North Kunlun, Middle Kunlun, and South Kunlun faults, respectively (Sun et al., 2009). The Heihaibei gold deposit is situated within the central part of the SKB (Fig. 1a). Two ophiolite belts are located along the Middle Kunlun fault and South Kunlun fault, and represent the suture zones of the Proto-Tethys and Paleo-Tethys, respectively (Yang et al., 1996).

The basement rocks exposed in the EKOB are intermediate to high-grade metamorphic rocks referred to as the Paleoproterozoic Jinshuikou and Kuhai Group, the Mesoproterozoic Xiaomiao Formation and the Meso-Neoproterozoic Wanbaogou Group (Wang et al., 2007). Among them, the Jinshuikou Group and Xiaomiao Formation are located in the NKB and the CKB; The Kuhai and Wanbaogou Groups are situated in the SKB (Dong et al., 2018). These basement rocks are overlain by Early Paleozoic low-grade metamorphic sedimentary and volcanic rocks that are unconformably overlain by the Devonian Maoniushan Formation (molasse) (Chen et al., 2014; Zhang et al., 2010). The Carboniferous-Middle Triassic strata mainly consist of marine and paralic clastic formations (Xiong, 2014; Chen et al., 2020). Of these, the intermediate to high-grade metamorphic rocks of the Paleoproterozoic Jinshuikou Group, the metasedimentary rocks of the Lower Triassic Bayankala Formation, and the sedimentary rocks of the Middle Triassic Naocangjiangou Formation host many of the Au-Sb deposits (Feng et al., 2009). The volcano-sedimentary rocks of the Sinian to Cambrian Wanbaogou and the Ordovician Nachitai Groups, both metamorphosed to greenschist facies, are the most important hosts of Co– and Cu-mineralization (Feng et al., 2009). Magmatic rocks are widespread in the EKOB and are dominated by granitoids, with minor mafic and ultramafic rocks (Chen et al., 2020). The mafic and ultramafic rocks occur mainly along the Central East Kunlun Suture Zone and Southern East Kunlun Suture Zone. The mafic and ultramafic rocks from the Central East Kunlun Suture Zone are dated to be Cambrian-Ordovician in age (537 Ma to 467 Ma) (Zhu et al., 2000; Bian et al., 2004; Li et al., 2013a; Qi et al., 2016). The granitoids include I-, S- and A-type units, which formed during two distinct emplacement episodes (470–380 Ma and 260–220 Ma) (Chen et al., 2017; Mo et al.,2007; Xiong et al., 2015) and display a temporal variation from early calc-alkaline granodiorites to late monzogranites and syenogranites in both episodes, respectively (Chen et al., 2016; Xiong et al., 2014; Xiong et al., 2015).

3. Geology of the mining area and geological characteristics of the ore bodies

3.1. Geology of the mining area

The Heihaibei gold deposit is located at Guolemude Town, near the Kunlun River, about 160 km southwest of the city of Golmud, Qinghai, NW China (Fig. 1a). The exposed strata of the Heihaibei gold deposit are mainly composed of the Meso-Neoproterozoic Wanbaogou and Ordovician-Silurian Nachitai Groups, of the Lower-Middle Triassic Naocangjiangou and Hongshuichuan Formation and Quaternary strata (Fig. 1c). The Wanbaogou Group mainly consists of siliceous and conglomeratic limestones, distributed in the southeast of the mining area. The Nachitai Group occurs mainly in the north of the mining area, and consists of metamorphic feldspar quartz sandstone and phyllite. The Hongshuichuan Formation comprises polymictic conglomerate and feldspathic graywacke and the Naocangjiangou Formation is composed of lithic arkose and siltstone, both of which are distributed mainly in the southwest of the mining area.

Structurally, there are two NW-SE-trending reverse faults in the mining area (Fig. 1c). $Fault_{52}$ is about 18 km long, 10–100 m wide and dips 25°-52° to the North, while $Fault_{53}$ is about 15 km long, 10–100 m wide and generally dips 30°-63° to the North (locally also dipping South) (Gu, 2017). $Fault_{52}$ runs through the Nachitai Group strata in the northern part of the mining area. Cataclasite, fault breccia, black fault gouge and quartz vein are developed in the fault zone, but the zone only displays little metal mineralization (Huang, 2018). $Fault_{53}$ is located in the central part of the mining area, and cataclasite, cataclastic monzogranite, fault breccia, fault gouge, quartz vein, pyritization and hydrothermal alteration are developed in the fault zone, while gold mineralization and massive pyritization only occur in the structural fissures within the monzogranite (Huang, 2018). Two episodes of magmatism are recognized in the central part of the mining area, and the main rock types of are monzogranite and gabbro that occur in stocks and dykes. The monzogranite unit is cut by the gabbro (Fig. 4d).

3.2. Geological characteristics of ore bodies

The Heihaibei gold deposit is comprised of six distinct ore bodies which have been identified by drilling efforts. The deposits yields a total reserve of 9.5 t Au with an average grade of 6 g/t (Huang, 2018). Most of the ore bodies strike east–west, and occur as lenticular within the monzogranite exposed in the central ore area (Fig. 1c). Ore body M1 hosts the major volume of the Au mineralization (Fig. 2). As evident from a prospecting trench in 2013, limonite and cataclasite are generally developed in the monzogranite and the gold grade in some sections is

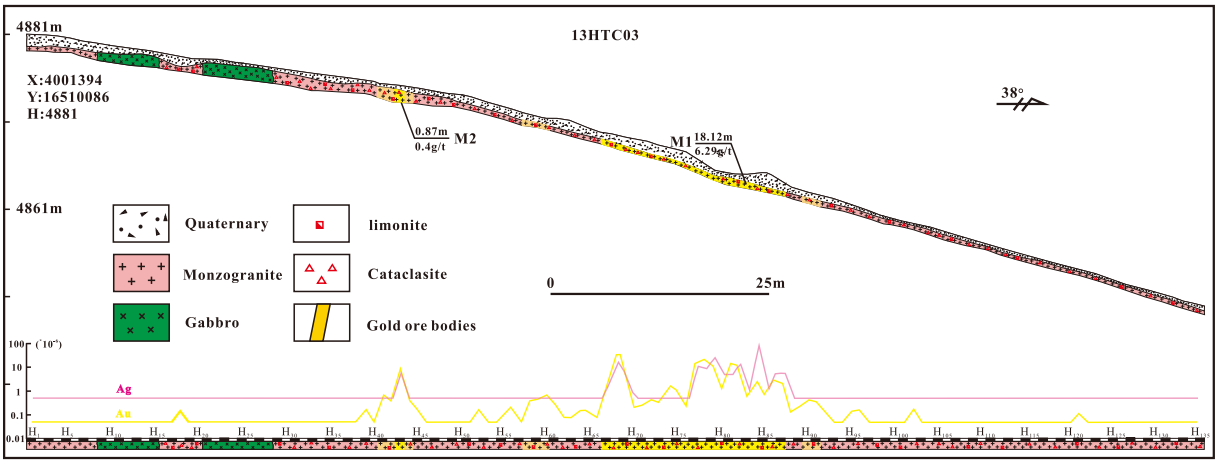

Fig. 3. 13HTC03 prospecting trench map showing the distribution characteristics of gold ore bodies and cross-cutting relationships between magmatic rocks in the Heihaibei gold deposit.

Table 2
The characteristics of gold ore bodies and monzogranites in the Heihiabei deposit.

Gold ore bodies numbers	Scale (m)		Au grade ($\times10^{-6}$)		Ore body morphology	Host rock	Occurrence	Data sources
	length	true thickness	the highest grade	the average grade				
M1	740	9.38	37.6	6.63	Lenticular	Monzogranites	189°∠78°	Huang et al., 2018;
M2	138	0.87	10.4	10.4	Lenticular	Monzogranites	183°∠85°	
M3	144	1.28	9.63	7.28	Lenticular	Monzogranites	183°∠80°	
M4	144	1.56	1.04	1.04	Lenticular	Monzogranites	11°∠75°	
M5	160	1.12	2.12	2.12	Lenticular	Monzogranites	11°∠75°	
M6	134	2.94	2.38	2.24	Lenticular	Monzogranites	0°∠75°	
Rock type	Mineral composition				Alternation	Characteristic texture		Data sources
Monzogranite	Plagioclase (30–35%), Perthite (20–25%), Microcline (5–10%), quartz (25–30%), Biotite (<5%)				Sericitization	Medium-grained,\Massive		This study

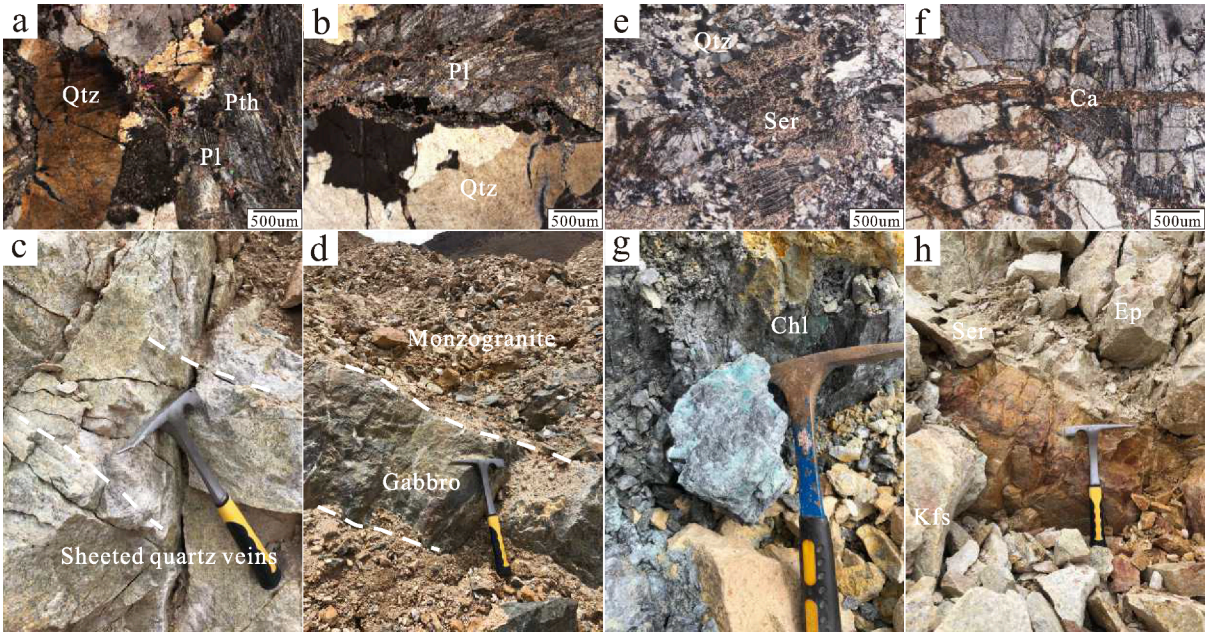

Fig. 4. (a-b) Photomicrographs of monzogranite; (c) Typical outcrop of auriferous sheeted veins from the monzogranite, (d) the gabbro dike cutting the monzogranite, (e) silicification and sericitization, (f) carbonation, (g) chloritization, (h) potassic alteration, sericitization and epidotization. Abbreviations are: Qtz: quartz; Pl: plagioclase; Pth: perthite; Kfs: K-feldspar; Ser: sericite; Chl: chlorite; Ca: calcite; Ep: epidote.

high to form gold ore body. The ore-bearing monzogranite and gold mineralized body is cut by the ore-barren gabbro (Figs. 2 and 3). The details of ore bodies and monzogranite characteristics are presented in Table 2 and Figs. 2 and 3, Fig. 4a and b.

Ore bodies M1, M2, and M3 have been characterized by their high economic grade, large thickness and constant exposure on the surface,

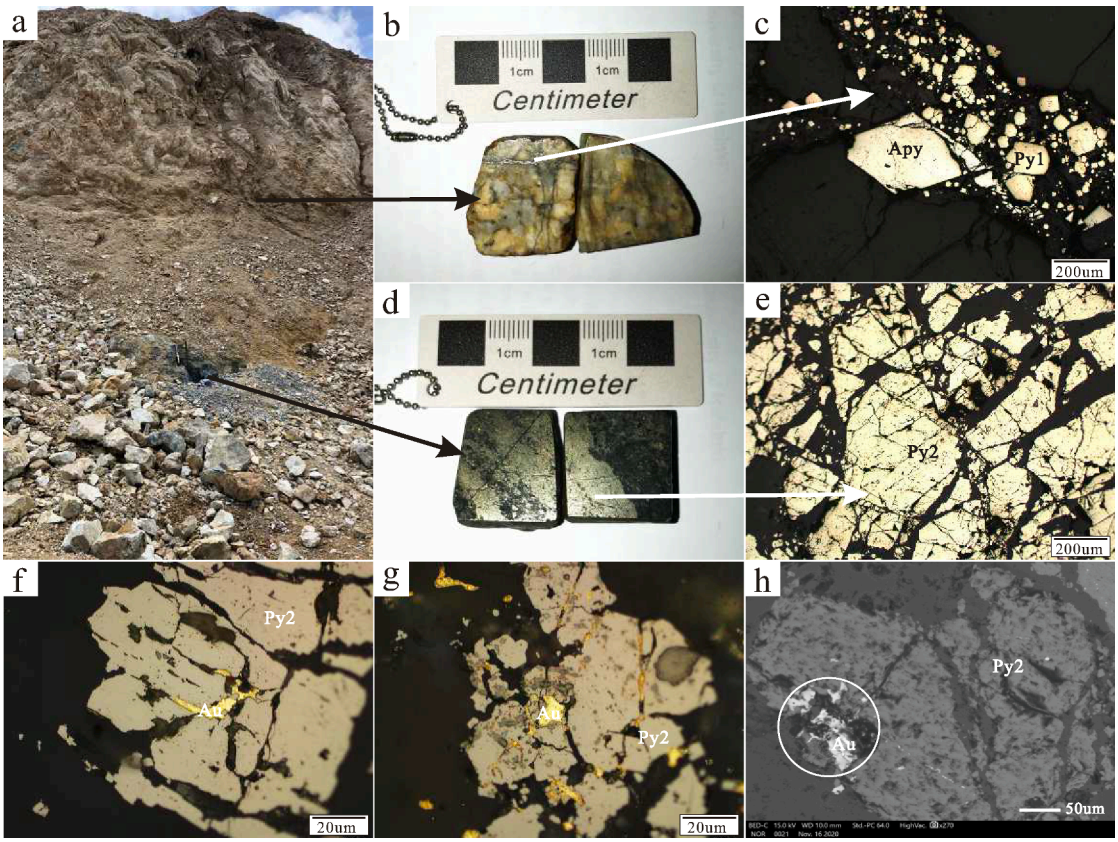

Fig. 5. (a-c) Monzogranite with veinlet disseminated pyrites (Py1) and arsenopyrites (Apy); (a, d, e) Dark quartz vein with laminated pyrites (Py2); (f-h) Native gold in laminated pyrites (Py2).

and by their low grade and thickness at depth, respectively. The gold resources in all three ore bodies are estimated to be 9457.19 kg (Fig. 2). Ore bodies M4, M5, and M6 are distributed in an echelon pattern, and are characterized by their relatively low grade, small thickness and patchy occurrence on the surface, whereas continuity and grade of these ore bodies tend to increase with depth. The total gold resources of these bodies are estimated to be 68.43 kg.

The Heihaibei gold deposit displays different types and degrees of hydrothermal alteration, including potassic alteration, silicification, sericitization, epidotization, chloritization, kaolinization and minor carbonation (Fig. 4e–h). The distribution of hydrothermal alteration is irregular and has no clear concentric zoning pattern. For the ore body M1, there are veinlet disseminated or fine stockwork pyrite, and sheeted arrays of parallel, low-sulfide, single stage quartz veins in the

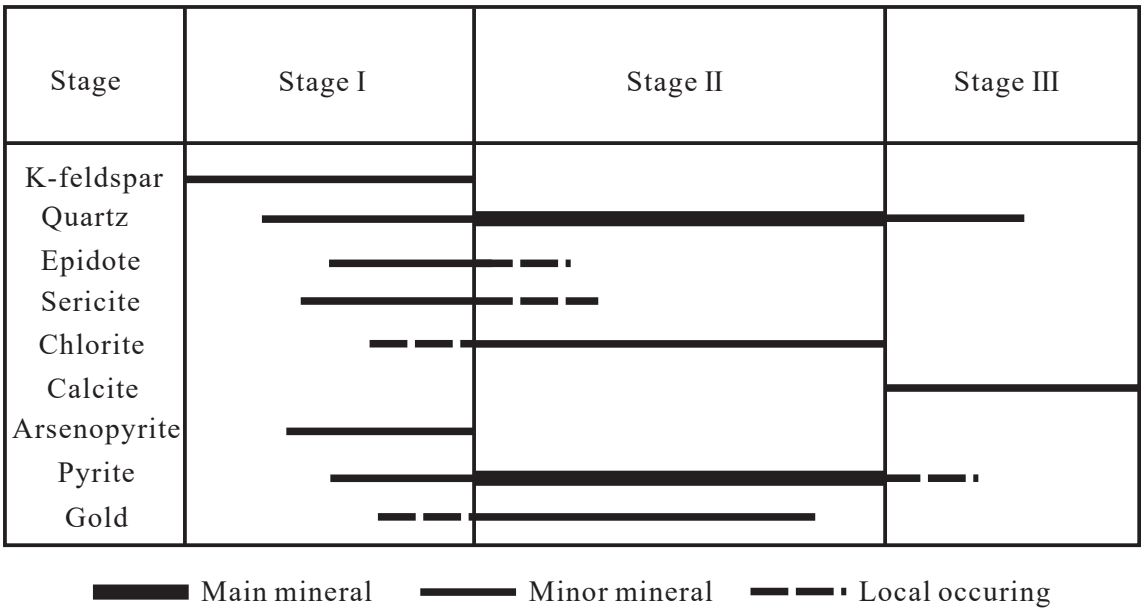

Fig. 6. Paragenetic sequence of mineralization and alteration in the Heihaibei gold deposit.

monzogranitic pluton's cupola (Fig. 4c; Fig. 9a; Fig. 5a–c). The wall rock alteration consists of potassic alteration, silicification, sericitization, and epidotization (Fig. 4e and h). Smoky grey quartz veins with high gold grades are mainly developed in the interior of monzogranite body, accompanied by massive pyrite and chloritization (Fig. 4g; Fig. 5a, d and e).

The main ore minerals are pyrite, arsenopyrite, and limonite, and native gold (Fig. 5). We group the pyrites from the Heihaibei gold deposit into two generations (Py1 and Py2), based on their mineral paragenetic associations, morphological and textural features. The first generation of pyrite (Py1) generally occurs as a veinlet disseminated or as a fine stockwork aggregation (Fig. 5b and c) and is associated with arsenopyrite, sericite and epidote, exhibiting a fine-grained (20–150 um in size) euhedral cubic texture. The second generation of pyrite (Py2), precipitated at the main metallogenic stage, has a size of 0.3 mm to 0.6 mm and occurs as a laminated aggregation or as a massive aggregation in the smoky grey quartz vein rich in fine grained sulfide (Fig. 5d and e). The Py2 comprises >90% of the total sulfides, and commonly occurs with quartz and chlorite. Native gold is mainly present in the form of fissure gold in Py2 (Fig. 5f–h). Gangue minerals include K-feldspar, quartz, plagioclase, sericite, epidote, chlorite, and calcite. The ores have massive, veined, disseminated, veinlet disseminated and fine stockwork structures. The textures of the ores include primarily euhedral-subhedral, allotriomorphic granular, and cataclastic textures.

Based on field research, cross-cutting relationships, mineral paragenetic associations, three stages for hydrothermal alteration and mineralization have been determined (Fig. 6): the K-feldspar-quartz-pyrite (Py1)-arsenopyrite-sericite-epidote stage (I) (Fig. 4e and h; Fig. 5b and c), the quartz-pyrite (Py2)-native gold-chlorite stage (II) (Fig. 4g; Fig. 5d–h), and the quartz-carbonate stage (III) (Fig. 4f).

4. Analytical methods

4.1. Zircon U-Pb dating and Hf isotopes

The monzogranite and gabbro exposed in the central part of the mining area were sampled for LA-ICP-MS zircon U-Pb geochronology (Sampling location: N 36°08.564′ E 93°06.655′, as shown in the Fig. 1c). Zircons were separated from whole-rock samples using conventional heavy liquid and magnetic techniques, and then by handpicking under a binocular microscope, at the Langfang Tuoxuan Rock and Mineral Testing Service Co., Ltd, Hebei Province, China. The handpicked zircons were examined under transmitted and reflected light with an optical microscope. To reveal their internal structures, cathodoluminescence (CL) images were obtained using a JEOL scanning electron microscope housed at the Langfang Tuoxuan Rock and Mineral Testing Service Co., Ltd, Hebei Province, China. LA-ICP-MS zircon U–Pb analyses were performed using an Agilent 7500a ICP-MS equipped with a 193 nm laser, housed at the Key laboratory of Mineral Resources Evaluation in Northeast Asia, Ministry of Land and Resources, Jilin University, China. Zircon 91,500 was used as an external standard and the NIST SRM 610 silicate glass was applied for instrument tuning. The laser diameter was 32 μm during the analyses. The instrument parameter and detail procedures were described by Yuan et al. (2004). The ICP-MS Data Cal (Ver. 6.7) and Isoplot (Ver. 3.0) programs were used for data reduction. Correction for common Pb was made following the technique described in Anderson (2002). Errors on individual analyses by LA-ICP-MS are provided at the 1σ level, while errors on pooled ages are given at the 95% (2σ) confidence level. The data are shown in Supplementary Table 1.

In-situ zircon Hf isotopes were measured using a Neptune Plus MC–ICP–MS instrument (Thermo Fisher Scientific, Germany) in combination with a Geolas HD excimer ArF LA system (Coherent, Göttingen, Germany) at the Wuhan Sample Analytical Technology Co., Ltd., Wuhan, China. Helium was used as the carrier gas within the ablation cell and was merged with argon after the ablation cell. All data were acquired in single-spot ablation mode using a spot size of 44 μm. Each measurement consisted of 20 s of background followed by 50 s of sample. Detailed operating conditions for the LA system and the MC–ICP–MS instrument are given by Hu et al. (2012). The data are shown in Supplementary Table 2.

4.2. Whole-rock major and trace elements

For geochemical analysis, whole-rock samples, after the removal of altered surfaces, were crushed in an agate mill to ~200 mesh. X-ray fluorescence (XRF; PW1401/10) using fused-glass disks and ICP-MS (Agilent 7500a with a shield torch) were used to measure the major and trace elements compositions, respectively, at the Key laboratory of Mineral Resources Evaluation in Northeast Asia, Ministry of Land and Resources, Jilin University, China., after acid digestion of samples in Teflon bombs. The analytical results for the AGV-2, BHVO-2, BCR-2 and RGM-2 standards indicate that the analytical precision for the major elements is better than 5%. For the trace elements the precision is generally better than 5% when the contents are >10 ppm, and better than 10% when concentrations are <10 ppm. The analytical results of major and trace elements are listed in Supplementary Table 3.

4.3. Fluid inclusion studies

Following detailed petrographic examination, micro-thermometric measurements were performed on a Linkam THMS-600 heating–freezing stage with a temperature range of −195 to +600 °C in the Key Laboratory of Geological Fluid, Jilin University, China. The equipment was calibrated by the freezing point of pure-water inclusions (0 °C) and the triple point of pure CO_2 inclusions (-56.6 °C). Measurement precisions are estimated as ± 0.2 °C at <30 °C, ±1 °C at 30–300 °C, and ± 2 °C at >300 °C. Ice-melting temperatures ($T_{m,\ ice}$), halite dissolution temperatures ($T_{m,\ d}$), and total homogenization temperatures (T_h) were measured. Heating and freezing rates were usually 1–5 °C min^{-1}, reducing to 0.1–0.5 °C min^{-1} as phase transitions were approached. Salinities are expressed as wt.% NaCl equiv. and were estimated from the melting temperatures of ice in aqueous (NaCl-H_2O) inclusions (Bodnar, 1993), using the data and methodology of Bodnar & Vityk (1994) for halite daughter mineral-bearing inclusions.

4.4. Trace element analysis of pyrite

Trace element analysis of pyrite in thin sections was conducted by LA-ICP-MS at Nanjing FocuMS Technology Co. Ltd. using a Teledyne Cetac Technologies Analyte Excite 193 nm ArF laser-ablation system (Bozeman, Montana, USA) connected to an Agilent Technologies 7700x quadrupole ICP-MS (Hachioji, Tokyo, Japan). The fluence used was 6 J/cm^2. A spot diameter of 40 μm and a 6 Hz repetition rate was used for 40 s signal (equating to 280 pulses) following a 15 s background. Raw data reduction was performed off-line using the ICP-MS Data Cal software using 100%-normalization strategy without applying internal standard (Liu et al, 2008). Helium was used as a carrier gas and Ar as a plasma gas mixed via a T-connector before entering the ICP-MS. The USGS polymetallic sulfide pressed pellet MASS-1 standard and the synthetic basaltic glass standard GSE-1G were used for correction of the sulfides. The data are shown in Supplementary Table 4.

4.5. Hydrogen and Oxygen isotopes

Oxygen isotopic compositions of quartz and hydrogen isotopic compositions of fluid inclusions (FIs) in quartz were analyzed at the Analytical Laboratory, Beijing Research Institute of Uranium Geology (BRIUG), Beijing, China National Nuclear Corporation. The analysis was conducted using a Finnigan MAT 253 mass spectrometer. The conventional BrF_5 method was used to determine O isotopic compositions (Clayton et al., 1972), and H isotopic compositions were determined

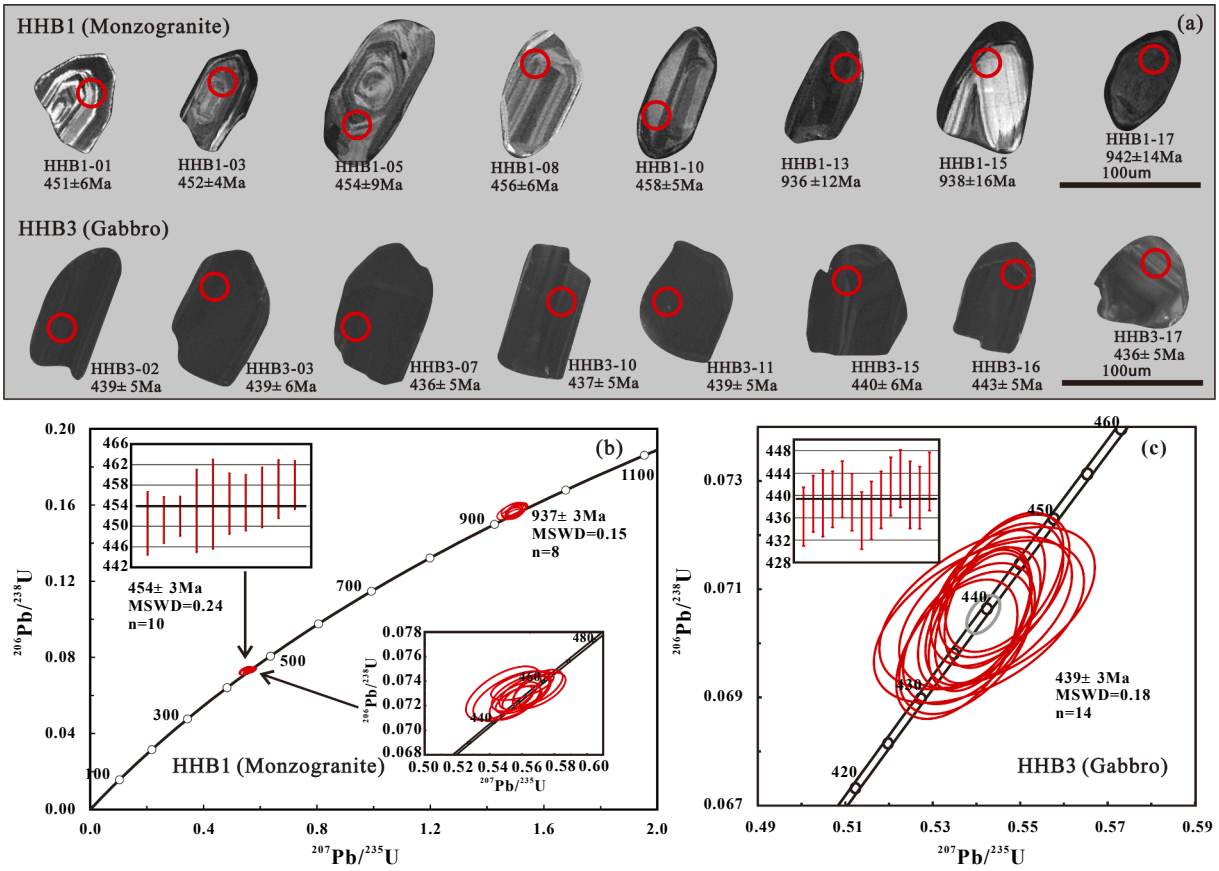

Fig. 7. Zircon U-Pb concordia diagrams and representative CL images for monzogranite and gabbro in the Heihaibei gold deposit.

using the Zn-reduction method (Coleman et al., 1982). The O and H isotopic values are reported in per mil relative to V-SMOW with analytical precisions of ± 0.2% for $\delta^{18}O_{quartz}$ and ± 0.2% for δD_{H2O}. The data are shown in Supplementary Table 5.

4.6. Sulphur and Lead isotopes

The S isotopic compositions and Pb isotopic ratios of samples (pyrite and arsenopyrite) were also analyzed at the BRIUG, Beijing. Sulfur isotopic compositions were determined using a Delta V plus mass spectrometer using the conventional combustion method (Robinson & Kusakabe, 1975). Results are reported as $\delta^{34}S$ relative to V-CDT with a reproducibility of ± 0.2‰. Lead isotope analyses were conducted using a Phoenix thermal ionization mass spectrometer. All Pb ratios were corrected according to the values of NBS SRM 981. Lead isotope analytical errors are reported as ± 2δ, and analytical precision was better than 0.005% for $^{208}Pb/^{206}Pb$ ratios. The data are shown in Supplementary Table 5.

5. Analytical results

5.1. U–Pb dating and Hf isotopic compositions of zircons

Zircons from the Heihaibei monzogranite have stubby columnar shapes (Fig. 7a), Th/U ratios of 0.11 to 0.72, and homogeneous internal structures, interpreted to reflect a magmatic origin (Supplementary Table 1). Ten analyzed zircon grains from the Heihaibei monzogranite yield a zircon U-Pb weighted mean age of 454 ± 3 Ma (MSWD = 0.24), and the remaining eight zircon grains give the older inherited ages of 931–944 Ma with a weighted mean age of 937 ± 8 Ma (MSWD = 0.15) (Fig. 7b). The T_{DM2} ages calculated from the corresponding εHf (t) values (−1.9 to 1.2) for the Late Ordovician zircon grains range from 1.36 Ga to 1.55 Ga (Fig. 8b and Supplementary Table 2). Inherited zircon grains with ages of 931–944 Ma have εHf (t) values from 0.1 to 4.2 corresponding to T_{DM2} ages ranging from 1.53 Ga to 1.79 Ga, respectively (Fig. 8b).

Most zircons from the Heihaibei gabbro are euhedral and show clear oscillatory growth zoning with Th/U ratios >0.1 (Fig. 7a; Supplementary Table 1), indicating a magmatic origin (Hoskin and Ireland, 2000). A total of 18 spots were analyzed on 18 zircon grains, and four spots were excluded due to low Th/U ratios (0.02–0.08), which could be caused by hydrothermal alteration or metamorphism. The remaining 14 spots yield weighted mean $^{206}Pb/^{238}U$ ages of 439 ± 3 Ma (MSWD = 0.18) (Fig. 7c), representing the formation age of the gabbro.

5.2. Whole-rock major and trace elements

All analyzed samples (Supplementary Table 3) plot into the granite field in a TAS discrimination diagram (Fig. 8a), and display high SiO_2 contents (74.4–81.4 wt%) and differentiation indices (DI = 91–96), corresponding in composition to fractionated granite. They are weakly peraluminous (molar A/CNK: $Al_2O_3/(CaO + Na_2O + K_2O) = 1.00–1.41$, with the majority of the samples having ratios of < 1.1; Fig. 8c), and display calc-alkalic affinities on a SiO_2-(Na_2O + K_2O-CaO) diagram (Fig. 8d).

These samples have low and variable total rare earth element (ΣREE) concentrations ranging from 15 to 329 ppm. They show relatively low zircon saturation temperatures (666–772 °C) (Supplementary Table 3), and negative Eu anomalies (Eu/Eu* = 0.26–0.83), except for one sample (HHB-Y1-1, with Eu/Eu* = 1.26), which could be due to the interaction between a melt and F/Cl rich fluids in the late stage of magmatic evolution (Muecke and Clarke, 1981; Jahn et al., 2001). All samples are

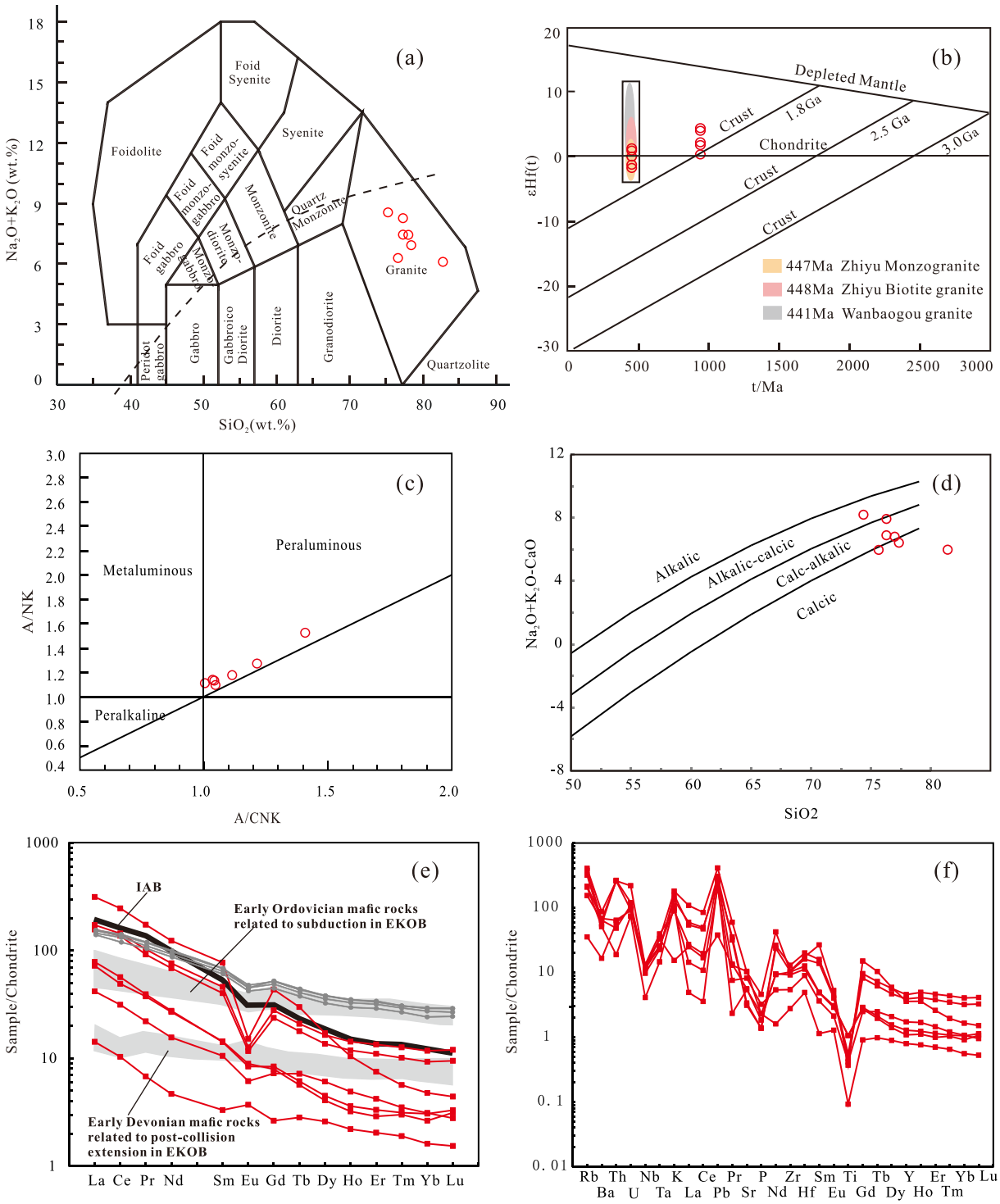

Fig. 8. (a) TAS classification diagram; (b) Zircon U-Pb ages vs. εHf(t) diagram (Zhou et al., 2016; Wang et al., 2012); (c) A/NK vs. A/CNK diagram (Chappell and White, 1974); (d) SiO_2 vs. $Na_2O + K_2O$-CaO diagram (Frost et al., 2001); (e-f) Chondrite-normalized REE patterns and primitive mantle-normalized element spider diagrams for monzogranite (red line) and gabbro (grey line) in the Heihaibei gold deposit (Sun and McDonough, 1989).

enriched in large-ion lithophile elements (LILEs; e.g. Rb, Th, U, and K) and depleted in high-field-strength elements (HFSEs; e.g. Nb, Ta, and Ti), with right-dipping rare earth element (REE) patterns (Fig. 8e and f).

5.3. Fluid inclusions

5.3.1. Fluid inclusion petrography

Representative samples of quartz veins from the K-feldspar-quartz-pyrite (Py1)-arsenopyrite-sericite-epidote stage (I) and the quartz-pyrite (Py2)-native gold-chlorite stage (II) were selected for fluid inclusion analysis. Petrographic studies showed that numerous primary Fluid Inclusions (FIs) formed during the hydrothermal metallogenic process of the Heihaibei gold deposit. The FIs occur randomly or regularly along growth bands or healed fissures in quartz, and were occasionally observed as isolated not connected to any structural weak zones in the minerals. These features are characteristic of primary FIs (Roedder,

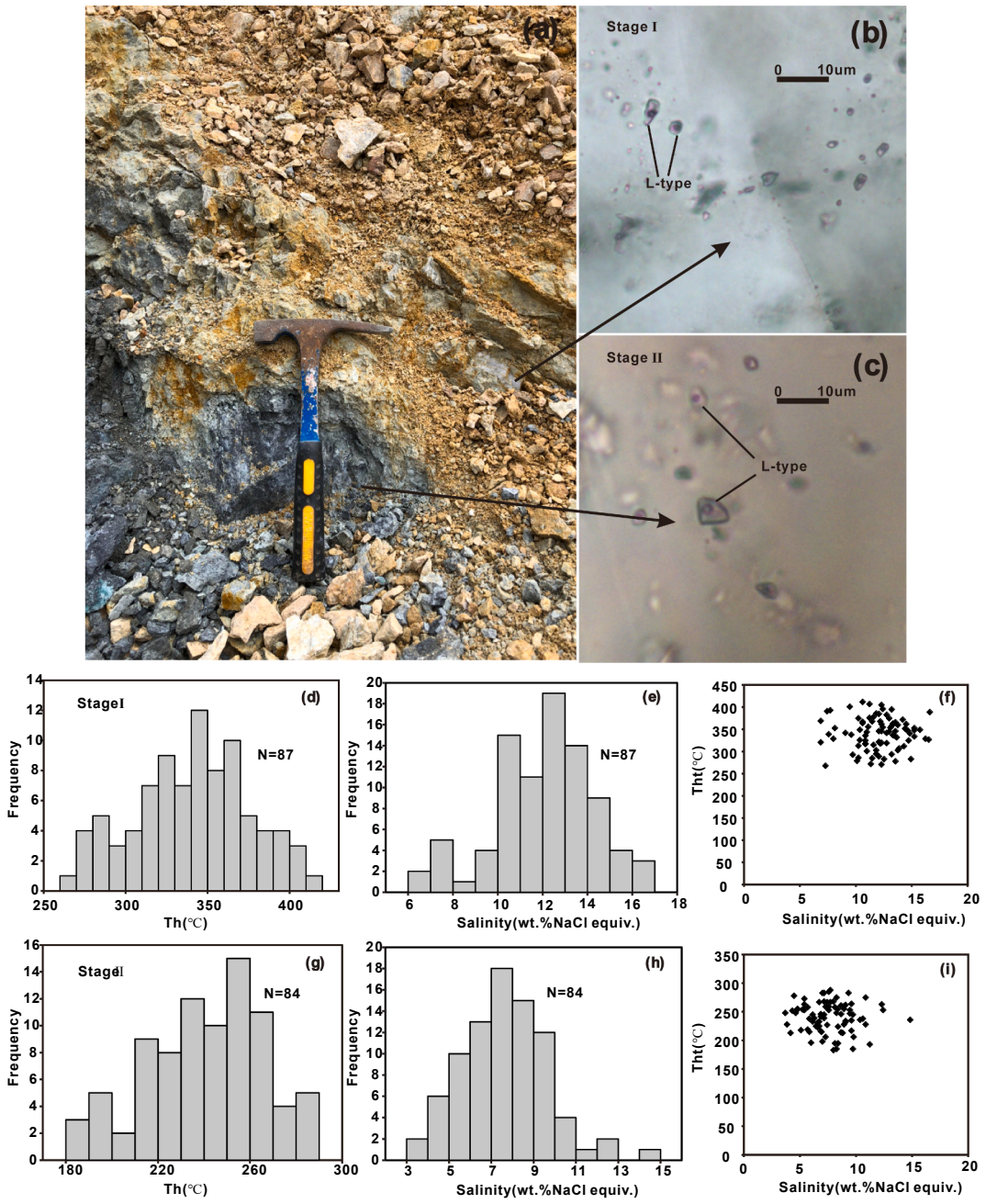

Fig. 9. (a-b) Distribution of fluid inclusions in the quartz veins from stage I; (a-c) Distribution of fluid inclusions in the quartz veins from stage II; (d-i) Histograms of homogenization temperatures (Th) and salinity for fluid inclusions analyzed.

1984). The primary FIs are classified as Liquid-rich two-phase aqueous FIs (L-type), recognized based on the phases that were present at room temperature (25 ℃) and the phase transformations that occurred from freezing to heating, as shown in Fig. 9a–c.

Liquid-rich two-phase aqueous FIs (L-type) contain a liquid phase and a vapor bubble at room temperature with a gas/liquid ratio of 15%-30%. These FIs ranged in size from 4 to 8 μm, exhibited round, elliptical and irregular shapes, occurred in isolation or as clusters along healed crystals, and homogenized to liquid during heating.

5.3.2. *Fluid inclusion micro-thermometry*

Here, we compare the temperature and salinity of the ore-forming fluids between the K-feldspar-quartz-pyrite (Py1)-arsenopyrite-sericite-epidote stage (I) and the quartz-pyrite-native gold-chlorite stage (II) using micro-thermometric results performed on FIs (L-type) of quartz veins. The micro-thermometric results for these FIs (L-type) are summarized in Fig. 9d–i.

The quartz veins from the K-feldspar-quartz-pyrite-arsenopyrite-sericite-epidote stage (I) display homogenization temperatures that range from 268 to 412 °C and occur dominantly in a range from 312 to 369 °C (Fig. 9d and f). The freezing points vary from −12.6 to −4.3 °C, which indicate that the salinities are in the range of 6.87–16.63 wt% NaCl equiv. (Fig. 9e and f). The salinities of the fluid inclusions in stage I mainly range from 10.1 to 14.9 wt% NaCl equiv.

The quartz veins from the quartz-pyrite-native gold-chlorite stage (II) have homogenization temperatures that range of 183–288 °C with most inclusions ranging from 213 to 268 °C (Fig. 9g and i). The freezing points range from −10.8 to −2.2 °C, and the salinities are in the range of 3.69–14.84 wt% NaCl equiv. The salinities of fluid inclusions in the stage II mostly range from 5.09 to 9.79 wt% NaCl equiv. (Fig. 9h, i). In

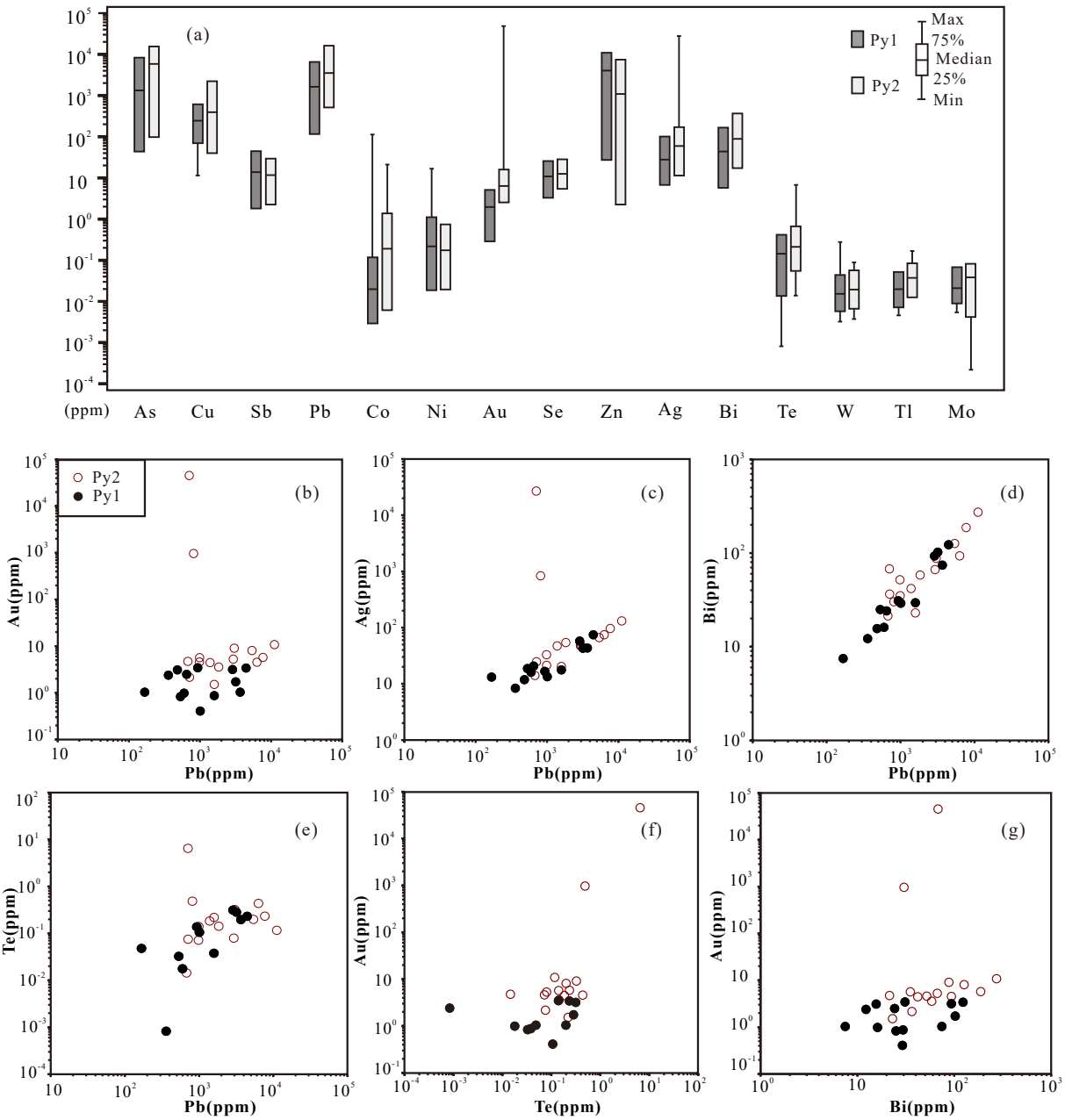

Fig. 10. (a) Boxplot showing the distribution of trace element concentrations in different pyrite types; (b-g) Scatter plots of trace elements for pyrites from the Heihaibei gold deposit. Analyses below detection limits are approximated at 50% of the detection limit.

general, the temperatures and salinities of the ore-forming fluids decrease gradually from stage I to stage II.

5.4. Trace element compositions of pyrite

LA-ICP-MS trace element analyses were conducted on Py1 grains for 13 spots and Py2 grains for 15 spots. The full analytical results are listed in Supplementary Table 4 and the distribution of element concentrations are illustrated in Fig. 10a.

Pyrites in the investigated samples contains consistently detectable Au (Py1: 0.41–3.46 ppm; Py2: 1.52–10.8 ppm). The Py2 grains generally have higher Au, As, Ag, Pb concentrations compared to Py1 (Fig. 10a). Reich et al. (2005) suggested that the lower temperatures may facilitate incorporation of Au, As and other trace elements in the crystal structure of the pyrites. We thus interpret the difference in trace element concentrations between Py1 and Py2 grains to result from different formation temperatures. A few spots of Py2 grains show very elevated concentrations of Au (45705 ppm), Ag (27060 ppm), Te (6.53 ppm), Se (18.6 ppm), and Bi (67.9 ppm). These elevated concentrations are likely related to discrete inclusions of gold and other sulfides. There are obvious positive correlations of Au, Ag, Te, and Bi with the Pb concentrations in Py1 and Py2 grains (Fig. 10b–e), and the Au-Bi, and Au-Te concentrations also show positive correlations (Fig. 10f and g).

5.5. Stable isotopic compositions

5.5.1. Hydrogen and oxygen isotopes

We analyzed the fluid H and O isotope compositions in one quartz sample from stage I and two quartz samples from stage II (Supplementary Table 5). The $\delta^{18}O_{V\text{-}SMOW}$ values range from 14.0 to 15.1 ‰. Based on the average homogenization temperatures of the corresponding FI assemblages and the fractionation formula ($1000\ln\alpha_{qtz\text{-}water}$ =

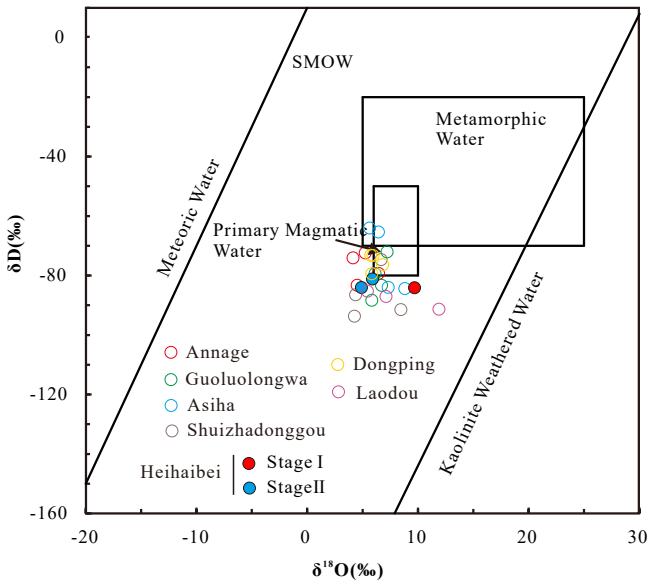

Fig. 11. Fluid δD and $\delta^{18}O$ characteristics of the Heihaibei gold deposit (after Sheppard, 1986).

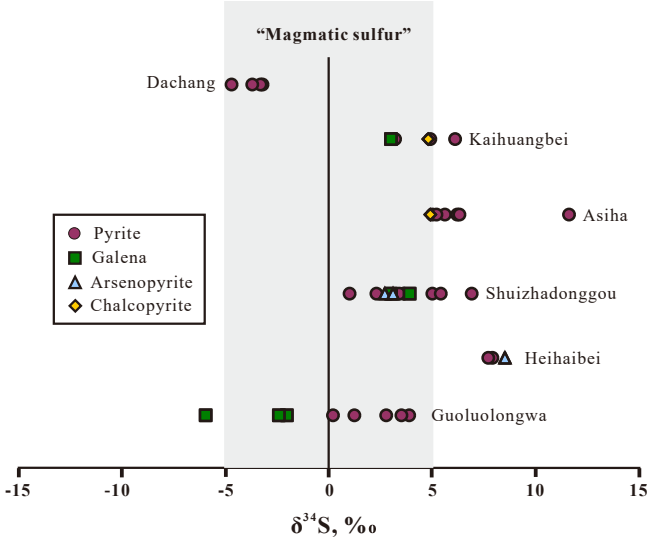

Fig. 12. The $\delta^{34}S$ values for minerals from the Heihaibei gold deposit and orogenic gold deposits in EKOB. $\delta^{34}S$ values of orogenic gold deposits are quoted from Li et al., (2017), Zhang et al., (2017) and Feng et al., (2002).

$3.38\times10^{6}T^{-2}$-3.40, Clayton et al., 1972), the calculated $\delta^{18}O_{H2O}$ values of the ore-forming fluids range from 4.9 to 9.7 ‰. The $\delta D_{V\text{-}SMOW}$ values range from −84.1 to −81.1‰. In a δD-$\delta^{18}O$ diagram (Fig. 11), the samples show proximity to or slightly deviate from the primary magmatic water field.

5.5.2. Sulfur and lead isotopes

We analyzed the S isotope compositions in three samples, including one arsenopyrite sample from stage I and two pyrite samples from stage II (Supplementary Table 5; Fig. 12). The $\delta^{34}S_{V\text{–}CDT}$ values of sulfides from the Heihaibei gold deposit range from 7.7 to 8.5‰, being relatively homogeneous and enriched in heavy S.

We also analyzed the Pb isotope compositions in three samples of pyrite from stage I and stage II (Supplementary Table 5; Fig. 13a and b). The Pb isotope compositions display small variations in $^{206}Pb/^{204}Pb$, $^{207}Pb/^{204}Pb$ and $^{208}Pb/^{204}Pb$, from 18.72 to 19.19, 15.69 to 15.71, and 38.73 to 39.24, respectively.

6. Discussion

6.1. Temporal relationships between gold mineralization, deformation and magmatism

The new U-Pb data suggest that the magmatic rocks in the Heihaibei deposit were emplaced episodically from 454 ± 3 to 439 ± 3 Ma. Field relationships between the magmatic rocks and the gold mineralization place important constraints on the age of the Heihaibei deposit. The gold ore bodies occur as lenticular in monzogranites, and the monzogranite zircons yield a weighted mean $^{206}Pb/^{238}U$ age of 454 ± 3 Ma. Zircons separated from gabbro dikes cutting through the monzogranites and gold mineralized body yield U-Pb ages of 439 ± 3 Ma. Hence, these U-Pb ages bracket the age of gold mineralization to between 454 ± 3 Ma and 439 ± 3 Ma.

There is now a broad consensus that the Proto-Tethys ocean opened no later than the Cambrian (Yang et al., 1996; Wei, 2015; Qi et al., 2016), however, the timing of closure time is still unclear. Mo et al. (2007) proposed that the blueschist and associated gabbro in the western segment of the EKOB marks the end of the subduction and the initiation of collision at 445 ± 2 Ma. Alternatively, oceanic crust subduction may have continued to the Early Silurian, based on the dating of a series of intrusive rocks which show geochemical affinities of arc magmatism and were considered to be associated with the late-stage of oceanic crust subduction (Li et al., 2013b; Wang et al., 2014; Zhang et al., 2014a; Hao et al., 2015).

Zhang et al. (2014a) proposed that the Santonggou granodiorite-diorite complex (432–427 Ma) was associated with the initiation of continental collision. In addition, the Bashierxi monzogranite has an emplacement age of 432 Ma, and is regarded as a product of continental collision following closure of the Proto-Tethys Ocean (Zheng et al., 2018). A large ductile East-West striking shear zone is developed in the Kunlun river area of the SKB, and its formation age is limited to an age range of 432 to 423 Ma by means of zircon U-Pb dating of deformed granodiorite and undeformed muscovite granite, which is regarded as the tectonic response of middle late Silurian collision orogeny (Gu et al., 2018). Meng and Zhang (2013) proposed that a high-pressure metamorphic belt is present along the central Kunlun fault zone, where eclogite has been identified with metamorphic zircons dated at 428 ± 2 Ma, providing further age constraints for the ocean closure. The 439 ± 3 Ma gabbro in the Heihaibei deposit shows slightly enriched Hf isotopic compositions (εHf(t) values, −3.2 to 0.1; unpublished data), and arc-like trace element patterns with an enrichment in LILEs (e.g., Rb, Th, U) and a depletion in HFSEs (e.g., Nb, Ta, Ti) (Fig. 8e and f). These rocks are comparable to mafic island arc rocks from the early Ordovician of the EKOB, but are different from those of the mafic rocks related to post-collision extension in the early Devonian of the EKOB (Niu and O'Hara, 2003; Cui et al., 2011; Liu et al., 2012; unpublished data). In addition, the coeval Huxiaoqin mafic rocks (438 Ma), Langmuri gabbro (438 Ma), and Qingshuiquan diabase dykes (436 Ma) were derived from an E-MORB-like mantle source, suggestive of a early Silurian back-arc rift setting related to the oceanic plate subduction (Liu et al., 2013; unpublished data; Ren et al., 2009). Hence, we suggest that subduction-related magmatism in the orogen probably continued until the early Silurian, and the gold mineralization in the Heihaibei deposit occurred in the subduction stage of the Early Paleozoic Proto-Tethys ocean.

6.2. Source of ore-forming fluids and materials

The characteristics of the Heihaibei gold deposit, including its alteration (silicification and sericitization), metallic element assemblage (Au + Ag + Sb + W), and fluid inclusions thermometric data (the main ore-forming temperature, 183–288 ℃), are consistent with those from orogenic gold deposits (Goldfarb et al., 2005) or are otherwise

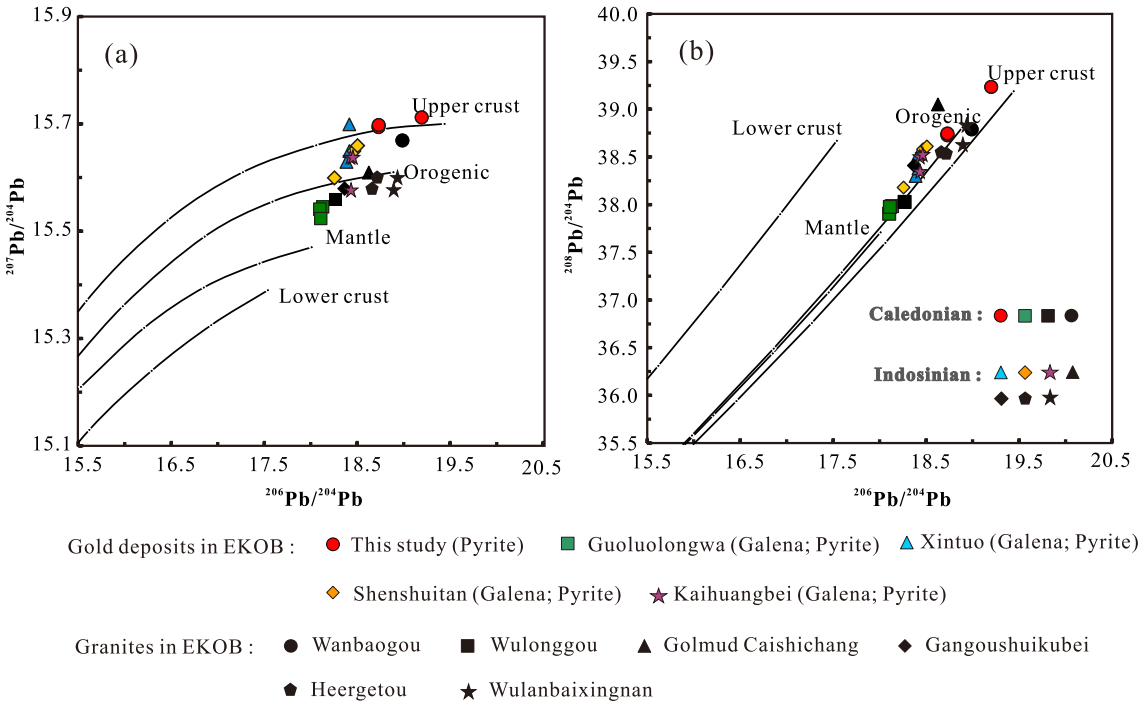

Fig. 13. Lead isotope composition of sulfides from the Heihaibei gold deposit. (a) $^{207}Pb/^{204}Pb$ vs. $^{206}Pb/^{204}Pb$. (b) $^{208}Pb/^{204}Pb$ vs. $^{206}Pb/^{204}Pb$. After Zartman and Doe (1981).

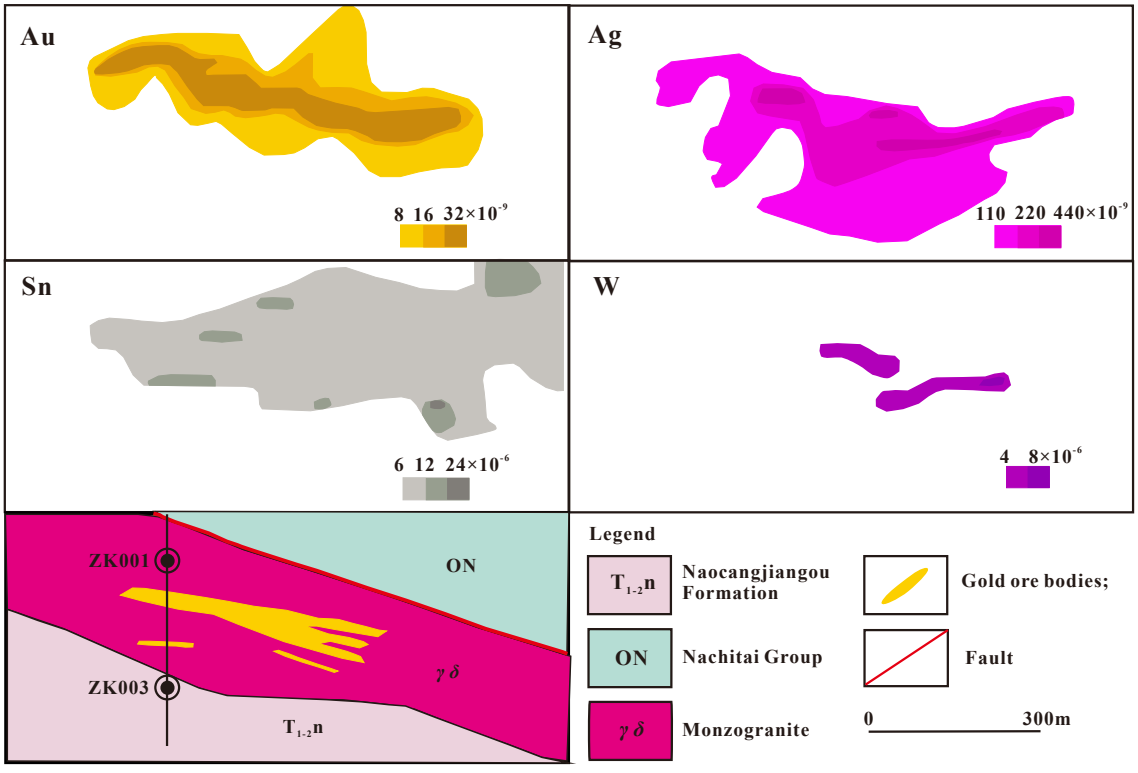

Fig. 14. The soil anomaly characteristics map in the Heihaibei gold deposit.

comparable to those of the proximal products of intrusion-related vein gold deposits (Sillitoe and Thompson, 1998; Lang and Baker, 2001). Goldfarb et al. (2005) and Lu et al. (2018) suggested that the ore-forming fluids for orogenic gold deposits were mainly derived from magmatic hydrothermal and metamorphic hydrothermal fluids, and their ore-forming materials are most likely from sedimentary strata. On the other hand, the ore-forming fluids and materials for IRGDs are considered to be dominated by a magmatic component (Lang and Baker, 2001; Hart et al., 2004). Integrating the following lines of evidence, we propose that the ore-forming fluids and materials for the Heihaibei deposit originate from a magmatic source.

Table 3
The $\delta^{34}S$ values for the minerals from the orogenic gold deposits in EKOB.

Deposit	Mineral	$\delta^{34}S$	References
Guoluolongwa	Pyrite	3.9	Li et al., 2017
	Pyrite	0.2	
	Pyrite	3.5	
	Pyrite	1.2	
	Pyrite	2.8	
	Galena	−6.0	
	Galena	−2.0	
	Galena	−2.4	
Shuizhadonggou	Pyrite	3.6	Zhang et al., 2017
	Pyrite	3.4	
	Arsenopyrite	2.7	
	Pyrite	2.3	
	Pyrite	1.0	
	Arsenopyrite	3.1	
	Pyrite	5.0	
	Galena	3.0	
	Pyrite	6.9	
	Pyrite	5.4	
	Galena	3.9	
Asiha	Pyrite	11.6	Li et al., 2017
	Pyrite	6.2	
	Pyrite	5.0	
	Pyrite	6.3	
	Pyrite	5.6	
	Chalcopyrite	4.9	
	Pyrite	5.2	
Kaihuangbei	Pyrite	6.1	Feng et al., 2002
	Pyrite	3.2	
	Pyrite	4.9	
	Chalcopyrite	4.8	
	Galena	3.0	
Dachang	Pyrite	−3.2	Feng et al., 2002
	Pyrite	−3.3	
	Pyrite	−4.7	
	Pyrite	−3.7	

6.2.1. Possible sources of sulfur

The lack of sulfate minerals in the Heihaibei ores suggests that the $\delta^{34}S_{V-CDT}$ value of sulfide can represent the total S isotope composition of the hydrothermal fluid, i.e. $\delta^{34}S_{\Sigma S} \approx \delta^{34}S_{sulfide}$ (Ohmoto, 1986). The S in the ore-forming fluids could originate from three main sources: (1) a mantle or magmatic source ($\delta^{34}S_{V-CDT} = 0 \pm 5‰$; Newberry et al., 1995;), (2) a marine/seawater source ($\delta^{34}S_{V-CDT} = \pm 20‰$), and (3) reduced S within sediments ($\delta^{34}S_{V-CDT} < 0$; Rollinson, 1993). The sulfides in the Heihaibei gold deposit show a narrow range of $\delta^{34}S_{V-CDT}$ values (7.7–8.5‰), which suggests: (1) relatively constant physico-chemical conditions of the mineralizing fluids during gold deposition (Li et al., 2012b), and (2) a common source of S (Saravanan and Mishra, 2009). These $\delta^{34}S_{V-CDT}$ values are slightly higher than the range of magmatic $\delta^{34}S_{V-CDT}$ values (Fig. 12), but still within the S isotopic composition range of typical granite reservoirs (−13.4 to +26.7; Zheng and Chen, 2000). Hou et al. (2004) and Vikent'eva and Prokofiev Vsevolod (2018) considered that the relatively high $\delta^{34}S_{V-CDT}$ values of sulfides combined with a relatively small variability were inherited from the host or source rock and reflect the assimilation of a large volume of these rocks into the ore assemblage. The Heihaibei gold ore bodies occurs as lenticular in the monzogranites, and the soil anomaly characteristics also show that Au, W and Sb anomalies mainly exist around the monzogranites (Fig. 14; Huang, 2018). Thus, we conclude that the high $\delta^{34}S$ values of the ore-forming fluids are probably derived from the Heihaibei monzogranites. The similar scenarios have also been proposed in the Xintuo-Haxiwa gold deposit in Qinghai (Zhang et al., 2018), Jinling and Xincheng gold deposits in Shandong (Liu et al., 2014; Zhang et al., 2014b).

6.2.2. Origin of ore-forming fluids

The stable O isotope data of the Heihaibei deposit have fluid $\delta^{18}O_{H2O}$ values and $\delta D_{v\text{-}smow}$ values comparable to those observed in EKOB orogenic gold deposits that have formed in magmatic-fluid systems (Guoluolongwa, Ding et al., 2013; Annage, Tao, 2014; Shuizhadonggou, Zhang et al., 2017; Asiha, Li et al., 2012a), and those of IRGDs, e.g., Dongping in the Heibei province (Bao et al., 2016) and Laodou lode in Xiahe-Hezuo district (Jin et al., 2017; Liu et al., 2000). These $\delta^{18}O_{H2O}$-$\delta D_{v\text{-}smow}$ values are situated close to the field of magmatic water (Fig. 11), indicating that the original fluids for these gold deposits may have had the same origin as the magmatic fluids. According to McCuaig and Kerrich (1998), fluid $\delta^{18}O_{H2O}$ values that are greater than +8‰ cannot be derived from magmatic fluids alone, and high $\delta^{18}O_{H2O}$ values in magmatic fluids are probably the result of fluid-rock interaction in the metavolcanic-sedimentary sequence (e.g. ^{18}O-enriched metasedimentary rocks) (e.g. Rogers et al., 2013; Bhattacharya et al., 2014). Notably, the higher $\delta^{18}O_{v\text{-}smow}$ values (and calculated $\delta^{18}O_{H2O}$ values) also occurs in Scheelite Dome and Clear Creek intrusion-related gold deposits, Yukon, reflecting isotopic exchange and interaction with the surrounding metasedimentary rocks (Mair et al., 2006; Marsh et al., 2003). Considering the geological background of the Heihaibei deposit, the Ordovician- Silurian Nachitai Group metamorphic rocks ($\delta^{18}O_{V\text{-}SMOW}$, 12.6–30.8; Guo et al., 2004) are likely candidates leading to the elevated $\delta^{18}O_{H2O}$ values of stage I. Therefore, we propose that the evolution of the ore-forming fluid at the Heihaibei gold deposit could be related to a magmatic-hydrothermal fluid, that possibly interacted with ^{18}O-rich metavolcanic-sedimentary rocks of the Nachitai Group during the early ore-forming stage.

6.2.3. Possible sources of lead

The $\delta^{34}S_{V-CDT}$ values of the EKOB orogenic gold deposits are generally in the "magmatic" range (0 ± 5‰), which suggests that magmatic sulfur might be the main S source of these Au ore-forming fluids (Table 3; Fig. 12). The Pb isotopes of the granites and orogenic gold deposits in the EKOB show similar distribution characteristics (Fig. 13; Zartman & Doe, 1981), and are mainly situated on the orogen evolution curves, suggesting a possible genetic link between orogenic gold deposits and the granitic magmatism (Zou et al., 2011; Zhang and Sun 2018; Feng and Zhang, 2002; Xu et al., 2020; Xu et al., 2020). Pyrite samples from the Heihaibei gold deposit also have Pb isotopic compositions similar to that of the Wanbaogou monzogranite (441 ± 5 Ma) in the SKB (Feng and Zhang, 2002), indicating a possible magma source. The Pb isotope data (Supplementary Table 5) indicate that the μ values ($^{238}U/^{204}Pb$ = 9.62 to 9.63) are between primitive mantle (μ_0 = 7.80) and crustal values (μ_c = 9.81), which reflects the isotope characteristics of a mixed Pb composition of crustal and mantle materials (Zhu et al., 1998). The Heihaibei monzogranites have relatively low Nb/Ta, Zr/Hf and relatively high La/Nb, and Ba/Nb values that are close to average crustal compositions (Taylor and Mclennan, 1985). The Hf isotopic composition (εHf(t) = -1.9 to + 1.2; TDM_2 = 1.36–1.55 Ga) also indicates that they were derived from Mesoproterozoic crust with a weak juvenile mantle-derived material signature. In addition, the observed Hf isotopic characteristics are similar to those of Late Ordovician (448–441 Ma) granitoids in the SKB (Fig. 8b; Wang et al., 2012; Zhou et al., 2016; Feng and Zhang, 2002), indicating the presence of Late Ordovician juvenile mantle-derived materials. These features are consistent with the isotope characteristics of a mixed Pb composition of crustal and mantle material in this study. Thus, we propose that Late Ordovician granitic magma was the source of Pb in the deposit.

According to Bierlein and McNaughton (1998) and Jin (2017), the Pb isotopic compositions of ore minerals in gold deposits can provide important constraints on the sources of the Pb and, by inference, Au and other metals in the hydrothermal fluids. Our new trace element data

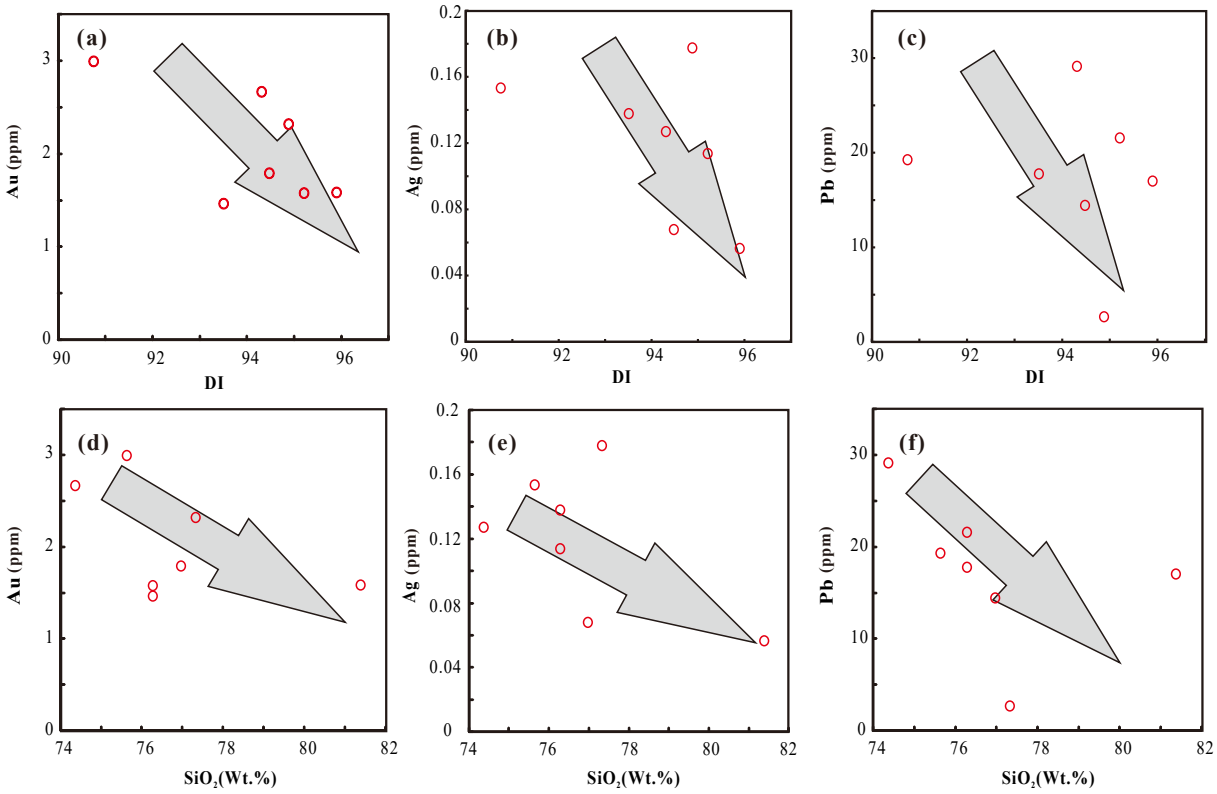

Fig. 15. (a) Au vs. DI, (b) Ag vs. DI, (c) Pb vs. DI, (d) Au vs. SiO_2, (e) Ag vs. SiO_2 and (f) Pb vs. SiO_2 diagrams for monzogranite.

provide additional evidence that the gold mineralization was related to the magmatism. The Pb in the ore-forming fluid is mostly of magmatic origin, while there are obvious correlations of Au, Ag, Te, and Bi with Pb concentrations (Fig. 10b–e) in the pyrites, which can be interpreted such that the magma has provided Pb and most of the other ore-forming metals. In addition, positive correlations between Au and Bi and between Au and Te (Fig. 10f and g) have also been identified from a variety of deposit types with Bi-Te geochemical signatures, especially in epithermal and related porphyry Cu-Au (e.g., Reich et al., 2013; Chapman et al., 2018), skarn Au (e.g., Meinert, 2000; Cepedal et al., 2006), intrusion-related Au (e.g., Cook et al., 2009; McCoy, 2000), magmatic Cu-Ni sulfide deposits (e.g., Helmy 2005), and VMS systems (e.g., Franchini et al., 2015). These types of deposits are all genetically associated with magmatism, indicating a magmatic source for Te, Bi, and Au.

6.3. Deposit type "orogenic" or "intrusion-related"

Several factors indicate that the Heihaibei gold deposit fits into the classification of Groves et al. (1998) for orogenic gold deposits. These include: (i) the lenticular gold orebodies occurs associated with quartz veins in the structural fissures of the granite; (ii) the hydrothermal mineral assemblage of the main metallogenic stage is in equilibrium (pressure and temperature) with the metamorphic conditions of greenschist facies; (iii) the ore-forming fluid is characterized by low-salinities (3.69 to 16.63 wt% NaCl equiv.). However, there are two distinct differences in the Heihaibei deposit with respect to this classification. Firstly, Feng et al. (2021) summarized the characteristics of orogenic gold deposits in the Kunlun river area, and considered that the NWW – to NW trending secondary faults are the main ore controlling structures and the age of gold mineralization is confined to the Triassic. A common feature of orogenic gold districts is the structural linking of the deposits to regional-scale faults or shear zones (Groves et al., 1998; Cox et al., 2001). The trend of faults in the Heihaibei deposit (F_{52} and F_{53}) are similar to the those in the Kunlun river area but the mineralization is significantly older. In addition, the occurrence of gold ore bodies is variable, and especially the dip direction of the main ore body M1 is opposite to that of the regional faults (F_{52}, F_{53}). Secondly, the age of the gold mineralization is between 454 ± 3 Ma and 439 ± 3 Ma, which is earlier than metamorphic peak and syn–to post–collisional magmatism (Meng and Zhang, 2013; Long et al., 2006; Liu et al., 2012). Goldfarb et al. (1998) and Kerrich et al. (2001) and Bierlein and Maher (2001) suggested that orogenic gold deposits are mostly controlled by regional secondary faults and form during or after the peak metamorphism of the *syn*-collisional orogeny. Regionally, two gold-mineralizing epochs for orogenic gold deposits are defined based on published Re-Os data (Late Devonian and Early Carboniferous; e.g., Chen et al., 2020), Ar-Ar dating and field observations (Middle-Late Triassic; e.g., Feng and Zhang, 2002; Zhang et al., 2017). Considering the geological background of the EKOB (Chen et al., 2017; Chen et al., 2020), the two gold mineralizing epochs should occur during the post-collisional stages related to the evolution of the Proto-Tethys Ocean and Paleo-Tethys Ocean, respectively.

The characteristics of IRGS deposits as compiled from Lang and Baker (2001), with contributions from Lang et al. (2000) and Thompson and Newberry (2000), are as follows: (i) reduced, sub-alkalic and metaluminous, intrusion of intermediate to felsic compositions that lie near the boundary between the ilmenite and magnetite series; (ii) intrusion-centered; (iii) small, shallow pluton; (iv) intrusion-related deposits are coeval with their associated, causative pluton; (v) low sulfide mineral contents, mostly <5 vol%, with a reduced ore mineral assemblage that typically comprises arsenopyrite, pyrrhotite and pyrite and lacks magnetite or hematite; (vi) areally restricted, commonly weak hydrothermal alteration; (vii) the pluton-proximal gold mineralization may be associated with elevated Bi, Te, and W aureole-hosted mineralization with As- or Sb-bearing ore, and the distal mineralization may be of Ag-Sb-Pb-Zn type; (viii) sheeted veins, stockworks, disseminations; and (ix) located in magmatic provinces best or formerly known for tungsten and/or tin deposits.

Our study shows that the Heihaibei deposit appears to share many characteristics with IRGS deposits. The most important and distinguishing features include: (i) the deposit is associated with the small elongate peraluminous intrusion of felsic compositions, (ii) the emplacement of the monzogranites and Au mineralization took place over a relatively short time span (ca. 454 to 439 Ma), (iii) the less systematic consistency in vein orientations, with most mineralization centered on intrusion cupolas, (iv) the soil anomaly characteristics show that the anomaly range of elements Au, Ag, Sn and W coincide approximately with the distribution range of monzogranite, suggesting it may be rock mass ore-control rather than structural ore-control (Fig. 14), (v) the metal zonation in which the pluton-proximal gold mineralization is associated with elevated W, and Sb concentrations, and the distal part is associated with a Pb-Zn enrichment (Huang, 2018), and (vi) there are sheeted arrays of parallel, low-sulfide, single-stage quartz veins in the monzogranitic pluton's cupola (Fig. 4c; Fig. 9a).

Nevertheless, some characteristics of the Heihaibei deposit distinguish it from typical IRGS deposits including: (i) the lenticular gold ore bodies occur associated with quartz veins in the structural fissures of the granite, (ii) abnormally high sulfide contents (local up to 80 vol%), and (iii) the monzogranites are peraluminous and lack evidence of reducibility. Although the Heihaibei deposit characteristics do not completely match those of typical IRGS deposits, there is a general consensus that magma is the main source of fluids, materials and energy in granite-related mineral systems (Cerny et al., 2005). We suggest that the ore-forming fluids and materials at the Heihaibei gold deposit were derived from a magmatic system, based on the metal signature, mineral association, isotopic evidence, and U-Pb data. This study also shows that the gold abundance in the Heihaibei monzogranite ($1.46 * 10^{-6} – 2.99 * 10^{-6}$) is much higher than the average gold abundance of magmatic rocks ($4.4 * 10^{-9}$) and crust ($3.5 * 10^{-9}$) globally (Ge at al., 1995). Moreover, as shown in Fig. 15, as the differentiation degree of granitic magma increases, the contents of Au, Ag and Pb in the residual siliceous melt decreases, indicating that there may be gold bearing fluid phase exsolution during diagenesis. The Heihaibei monzogranites were fractionated granite derived from partial melting of Mesoproterozoic crust with involvement of some juvenile mantle-derived components, and formed in the subduction stage of the Early Paleozoic Proto-Tethys ocean. Zhang and Sun (2018) demonstrated the existence of upper mantle gold source in East Kunlun, and consequently, that the addition of mantle derived components may lead to the enrichment of Au and other associated metals. In addition, Fortin et al., (2015) and Liu et al., (2021) suggested that high pressure and water rich environment is conducive to improve the solubility of Au and S in magma. A high oxidation fugacity prevents early formation of sulphide globules in a magma, which can increase Au abundance in the residual melt during fractionation (Candela, 1989). In summary, we suggest that the Heihaibei monzogranite has great gold mineralization potential. A number of early to middle Triassic gold deposits have also been reported to be mainly associated with subduction-related magmatism in the adjacent western Qinling region, e.g., the Laodou lode and (Jin et al., 2017) and Zaozigou deposits (Sui et al., 2017).

The Heihaibei gold deposit investigated in this study shares many characteristics with orogenic gold deposits and IRGS deposits. Based on the above discussion, we conclude that the deposit may instead be classified as a granitic intrusion-related gold deposit. However, as a a newly discovered gold deposit in the EKOB, the exploration degree of the Heihaibei gold deposit is yet relatively low. The IRGS is a relatively recently defined deposit classification, and the physical characteristics and genetic processes that operated in it still need intensive study.

7. Conclusion

(1) The Heihaibei gold mineralization occurred in the subduction stage of Early Paleozoic Proto-Tethys ocean, and its age is limited between 454 Ma and 439 Ma.

(2) The ore-forming fluid and materials were derived from a magmatic-hydrothermal source, and closely related to Heihaibei monzogranites.

(3) Compared with the typical characteristics of orogenic gold deposits and IRGS deposits, the Heihaibei gold deposit may instead be classified as a granitic intrusion-related gold deposit.

Declaration of Competing Interest

The authors declare that they have no known competing financial interests or personal relationships that could have appeared to influence the work reported in this paper.

Acknowledgements

We thank the editor for his patience in dealing with our manuscript and thank the anonymous reviewers for their critical but constructive comments, which have significantly improved an earlier version of the manuscript. We acknowledge the helpful staff in the Key laboratory of Mineral Resources Evaluation in Northeast Asia, Ministry of Land and Resources of China and Wuhan Sample solution Analytical Technology Co., Ltd., Wuhan, China to help us analyze and handle the samples. This work was financially supported by the Geological Surveying Project of Geological Survey Party sponsored by the Geological Survey Bureau of China [No. 12120114080801]. Yu L. acknowledges support from the Chinese Scholarship Council for a research stay at the University of Helsinki.

Appendix A. Supplementary data

Supplementary data to this article can be found online at https://doi.org/10.1016/j.oregeorev.2022.104859.

References

Anderson, T., 2002. Correction of common lead in U-Pb analyses that do not report 204Pb. Chem. Geol. 192, 59–79.

Bian, Q.T., Li, D.H., Pospelov, I., et al., 2004. Age, geochemistry and tectonic setting of Buqingshan ophiolites, North Qinghai-Tibet Plateau. China. J. Asian Earth Sci. 23, 577–596.

Bodnar, R.J., 1993. Revised equation and table for determining the freezing point depression of H2O-NaCl solutions. Geochem. Cosmochim. Acta 57, 683–684.

Bodnar, R.J., Vityk, M.O., 1994. Interpretation of microthermometric data for H2O-NaCl fluid inclusions. In: de Vivo, B., Frezzotti, M.L. (Eds.), Fluid Inclusions in Minerals, Methods and Applications. Virginia Tech, Blacksburg, VA, pp. 117–130.

Bhattacharya, S., Panigrahi, M.K., et al., 2014. Oxygen isotope ratio of quartz veins from the auriferous Ramagiri-Penakacherla schist belt and surrounding granitoids in the Eastern Dharwar craton: a case for a possible link between gold mineralization and granite magmatism. Ore Geol. Rev. 63, 201–208.

Bierlein, F., McNaughton, N., 1998. Pb isotope fingerprinting of mesothermal gold deposits from central Victoria, Australia: implications for ore genesis. Miner. Deposita 33, 633–638.

Bierlein, F.P., Maher, S., 2001. Orogenic disseminated gold in phanerozoic fold belts-examples from Victoria. Australia and elsewhere. Ore Geol. Rev. 18 (1–2), 113–148.

Bao, Z.W., Li, C.J., Zhao, Z.H., 2016. Metallogeny of the syenite-related Dongping gold deposit in the northern part of the North China Craton: A review and synthesis. Ore Geology Reviews 73, 198–210.

Chen, J.J., Fu, L.B., et al., 2020. Multiple episodes of gold mineralization in the East Kunlun Orogen, western Central Orogenic Belt, China: Constraints from Re-Os sulfide geochronology. Ore Geol. Rev. 123 (2020), 103587.

Chen, Y.X., Pei, X.Z., Li, R.B., et al., 2014. Geochemical characteristics and tectonic significance of meta-sedimentary rocks from Naij Tal group, eastern section of East Kunlun. Geosci. 28, 489–500.

Chen, J., Wei, J., Fu, L., Li, H., et al., 2017. Multiple sources of the early Mesozoic Gouli batholith, Eastern Kunlun Orogenic Belt, northern Tibetan Plateau: linking continental crustal growth with oceanic subduction. Lithos 292–293, 161–178.

Chen, J.J., Fu, L.B., Wei, J.H., et al., 2016. Geochemical characteristics of late Ordovician granodiorite in Gouli area, Eastern Kunlun Orogenic Belt, Qinghai province: implications on the evolution of Proto-Tethys Ocean. Earth Sci. 41 (11), 1863–1882 in Chinese with English abs.

Candela, P. A. 1989. Felsic magmas, volatiles and metallogenesis. In Whitney, J. A. & Naldrett, A. J. (eds) Ore Deposits Associated With Magmas. Rev. Econ. Geol. 4, 23-33.

Clayton, R.N., O'Neil, J.R., Mayeda, T.K., 1972. Oxygen isotope exchange between quartz and water. J. Geophys. Res. 77, 3057–3067.

Coleman, M.L., Sheppard, T.J., et al., 1982. Reduction of water with zinc for hydrogen isotope analysis. Anal. Chem. 54, 993–995.
Chapman, R.J., Allan, M.M., et al., 2018. A new indicator mineral methodology based on a generic Bi-Pb-Te-S mineral inclusion signature in detrital gold from porphyry and low/intermediate sulfidation epithermal environments in Yukon Territory. Canada. Miner. Deposita 53, 815–834.
Cepedal, A., Fuertes-Fuente, M., et al., 2006. Tellurides, selenides and Bi-mineral assemblages from the Rio Narcea Gold belt, Austrias, Spain: genetic implications in Cu-Au and Au skarn. Mineral Petrolol. 87, 277–304.
Cook, N.J., Ciobanu, C.L., Mao, J.W., 2009. Textural control on gold distribution in As-free pyrite from the Dongping, Huangtuliang and Hougou gold deposits, North China craton (Hebei Province, China). Chem. Geol. 264, 101–121.
Cerny, P., Blevin, P.L., Cuney, M., Nicolescu, S., 2005. Granite-related ore deposits. Econ. Geol. 100th Anniversary Volume, 337–370.
Cui, M.H., Meng, F.C., et al., 2011. Early Ordovician island arc of Qimantag Mountain, eastern Kunlun: Evidences from geochemistry, Sm-Nd isotope and geochronology of intermediate-basic igneous rocks. Acta Petrologica Sinica 27 (11), 3365–3379.
Cox, S.F., Knackstedt, M.A., Braun, J., 2001. Principles of structural control on permeability and fluid flow in hydrothermal systems. Society of Economic Geologists Reviews 14, 1–24.
Ding, Q.F., Jin, S.K., Wang, G., Zhang, B.L., 2013. Ore-forming fluid of the Guoluolongwa gold deposit in Dulan County, Qinghai Province. J. Jilin Univ. (Earth Sci. Ed.) 43, 415–426 in Chinese with English abstract.
Dong, G.C., Luo, M.F., et al., 2018. Petrogenesis and tectonic implications of early Paleozoic granitoids in East Kunlun belt: Evidences from geochronology, geochemistry and isotopes. Geosci. Front. 9 (2018), 1383–1397.
Feng, C.Y., Zhang, D.Q., 2002. Multiple orogenic processes and mineralization of orogenic gold deposits in the East Kunlun Orogen, Qinghai province. Chinese Academy of Geological Sciences, China. Ph.D thesis.
Feng, C.Y., Qu, W.J., et al., 2009. Re-Os dating of pyrite from the Tuolugou stratabound Co(Au) deposit, eastern Kunlun Orogenic Belt, northwestern China. Ore Geol. Rev. 36 (2009), 213–220.
Franchini, M., McFarlane, C., et al., 2015. Trace metals in pyrite and marcasite from the Agua Rica porphyry-high sulfidation epithermal deposit, Catamarca, Argentina: textural features and metal zoning at the porphyry to epithermal transition. Ore Geol. Rev. 66, 366–387.
Fortin, M.A., Riddle, J., et al., 2015. The effect of water on the sulfur concentration at sulfide saturation (SCSS) in natural melts. Geochim Cosmochim Acta 160, 100–116.
Feng, L.Q., Gu, X.X., et al., 2021. Genesis of the gold deposits in the Kunlun River area, East Kunlun, Qinghai Province: Constraints from geology, fluid inclusions and isotopes. Ore Geology Reviews 139 (2021) 104564 Available.
Gu, X.X., 2017. Metallogenic regularity and prospecting direction of gold deposits in Kunlun river area. China University of Geosciences (Beijing) (in Chinese), Qinghai Province.
Gu, X.X., Zhang, Y.M., Feng, L.Q., 2018. Recognition, age determination and tectonic significance of the Kunlun River ductile shear zone in the East Kunlun Mountains. Geological Bulletin of China, 2018, 37(2/3): 345-355.
Guo, X.P., Wang, N.W., et al., 2004. Geochemical divergence between the matrix system and exotic block system in the Naij Tai and Wanbaogou groups in the East Kunlun Mountains. Geochemical bulletin of China 23, 1188–1195.
Goldfarb, R.J., Groves, D.I., 2015. Orogenic gold: Common or evolving fluid and metal sources through time. Lithos 233, 2–26.
Goldfarb, R.J., Baker, T., Dubé, B., Groves, D.I., Hart, C.J.R., Gosselin, P., 2005. Distribution, character, and genesis of gold deposits in metamorphic terranes. Econ. Geol. 100th Anniv, 407–450.
Goldfarb, R.J., Groves, D.I., Gardoll, S., 2001. Orogenic gold and geologic time: a global synthesis. Ore Geol. Rev. 18, 1–75.
Groves, D.I., Santosh, M., Deng, J., Wang, Q., Yang, L., Zhang, L., 2020. A holistic model for the origin of orogenic gold deposits and its implications for exploration. Miner. Deposita 55, 275–292.
Groves, D.I., Goldfarb, R.J., et al., 1998. Orogenic gold deposits: A proposed classification in the context of their crustal distribution and relationship to other gold deposit types. Ore Geol. Rev. 13 (1–5), 7–27.
Goldfarb, R.J., Phillips, G.N., et al., 1998. Tectonic setting of synorogenic gold deposits of the Pacific Rim. Ore Geol. Rev. 13 (1–5), 185–218.
Hart, C.J.R., Goldfarb, R.J., et al., 2004. The North Cordilleran Mind-Cretacesous plutonic provinces: ilmenite/magnetite-series granitoids and intrusion related mineralization. Resour. Geol. 54, 253–280.
Huang, G.B., 2018. Preliminary investigation report of Heihaibei gold deposit in Golmud City. Bureau of Geological Exploration & Development of Qinghai Province, Qinghai Province in Chinese.
Hu, Z., Liu, Y., Gao, S., Liu, W., et al., 2012. Improved in situ Hf isotope ratio analysis of zircon using newly designed X skimmer cone and jet sample cone in combination with the addition of nitrogen by laser ablationmultiple collector ICP-MS. J. Anal. At. Spectrom. 27 (9), 1391–1399.
Hou, M.L., Ding, X., et al., 2004. Lead and sulfur isotope geochemistry of the Hexi gold deposit in Penglai, eastern Shandong. Acta Geoscien Tica Sinica 25 (2), 145–150 in Chinese with English abstract.
Helmy, H.M., 2005. Melonite-group minerals and other tellurides from three Cu-Ni-PGE prospects, Eastern Desert. Egypt. Ore Geol. Rev. 26, 305–324.
Hao, N.N., Yuan, W.M., Zhang, A.K., Feng, Y.L., Cao, J.H., Chen, X.N., Chen, X.Q., Mo, X. X., 2015. Evolution process of the Late Silurian-Late Devonian tectonic environment in Qimantagh in the western portion of east Kunlun, China: evidence from the geochronology and geochemistry of granitoids. J. Earth Syst. Sci. 124 (1), 171–196.
Jahn, B.M., Wu, F., Capdevila, R., Martineau, F., Zhao, Z., Wang, Y., 2001. Highly evolved juvenile granites with tetrad REE patterns: the Woduhe and Baerzhe granites from the Great Xing'an Mountains in NE China. Lithos 59, 171–198.
Jin, X.Y., Li, J.W., et al., 2017. Magmatic-hydrothermal origin of the early Triassic Laodou lode gold deposit in the Xiahe-Hezuo district, West Qinling orogen, China: implications for gold metallogeny. Miner Deposita 2017 (52), 883–902.
Kerrich, R., Goldfarb, R., Groves, D., et al., 2001. The characteristics, origins and geodynamic settings of supergiant gold metallogenic provinces. Science in China (series D) 43 (Sup.), 1–68.
Li, R.B., Pei, X.Z., Li, Z.C., et al., 2013a. Geochemical features, age, and tectonic significance of the Kekekete mafic-ultramafic rocks, East Kunlun Orogen. China. Acta Geol. Sin. 87, 1319–1333.
Li, W., Neubauer, F., Liu, Y.J., Genser, J., Ren, S.M., Han, G.Q., Liang, C.Y., 2013b. Paleozoic evolution of the Qimantagh magmatic arcs, Eastern Kunlun Mountains: constraints from zircon dating of granitoids and modern river sands. J. Asian Earth Sci. 77 (21), 183–202.
Liu, K., Zhang, L., et al., 2021. Effects of sulfide composition and melt H_2O on sulfur content at sulfide saturation in basaltic melts. Chem Geol 559, 119913.
Liu, Y.S., Hu, Z.C., et al., 2008. In situ analysis of major and trace elements of anhydrous minerals by LA-ICP-MS without applying an internal standard. Chem. Geol. 257 (1–2), 34–43.
Liu, B., Ma, C.Q., et al., 2013. Early Paleozoic tectonic transition from ocean subduction to collisional orogeny in the Eastern Kunlun region: Evidence from Huxiaoqin mafic rocks. Acta Petrologica Sinica 29 (6), 2093–2106.
Lang, J., Baker, T., 2001. Intrusion-related gold systems: the present level of understanding. Miner. Deposita 36, 477–489.
Li, B.L., Shen, X., Chen, G.J., et al., 2012a. Geochemical features of ore-forming fluids and metallogenesis of vein I in Asiha gold ore deposit, Eastern Kunlun. Qinghai Province. Journal of Jilin University (Earth Science Edition) 42 (6), 1676–1687.
Li, J.W., Bi, S.J., Selby, D., et al., 2012b. Giant Mesozoic gold provinces related to the destruction of the North China craton. Earth Planet. Sci. Lett. 349, 26–37.
Long, X.P., Jin, W., Ge, W.C., Yu, N., 2006. Zircon U-Pb geochronology and geological implications of the granitoids in Jinshuikou, East Kunlun, NW China. Geochimica 35, 333–345 in Chinese with English abstract.
Liu, B., Ma, C.Q., Zhang, J.Y., Xiong, F.H., Huang, J., Jiang, H.A., 2012. Petrogenesis of Early Devonian intrusive rocks in the east part of Eastern Kunlun Orogen and implication for Early Palaeozoic orogenic processes. Acta Petrol. Sin. 28 (6), 1785–1807.
Lang, J.R., Baker, T., Hart, C.J.R., Mortensen, J.K., 2000. An exploration model for intrusion related gold systems. Econ. Geol. Newslett. 40, 1–15.
Lu, H.Z., Chi, G.X., Zhu, X.Q., 2018. Geological Characteristics and Ore Forming Fluids of Orogenic Gold Deposits. Geotectonica et Metallogenia 42 (2), 244–265.
Mo, X.X., Luo, Z.H., Deng, J.F., et al., 2007. Granitoids and crustal growth in the East-Kunlun Orogenic Belt. Geol. J. China Univ. 13 (03), 403–414 in Chinese with English abs.
Muecke, G.K., Clarke, D.B., 1981. Geochemical evolution of the South Mountain Batholith, Nova Scotia; rare-earth-element evidence. The Canadian Mineralogist (1981) 19 (1): 133–145.
Meng, F.C., Zhang, J.X., 2013. Discovery of Early Paleozoic eclogite from the East Kunlun, Western China and its tectonic significance. Gondwana Res. 23 (2013), 825–836.
McCuaig, T.C., Kerrich, R., 1998. P-T-t-deformation-fluid characteristics of lode gold deposits: evidence from alteration systematics. Ore Geol. Rev. 12, 381–453.
Meinert, L.D., 2000. Gold in skarn related to epizonal intrusions. Rev. Econ. Geol. 13, 347–375.
McCoy, D.T., 2000. Mid-Cretaceous Plutonic-related Gold Deposits of Interior Alaska: Metallogensis, Characteristics, Gold Associative Mineralogy and Geochronology. University of Alaska, Fairbanks, p. 245. Ph.D thesis.
Mernagh, T.P., Bastrakov, E.N., Zaw, K., Wygralak, A.S., Wyborn, L.A.I., 2007. Comparison of fluid inclusion data and mineralization processes for Australian orgenic gold and intrusion-related gold systems. Acta Petrol. Sin. 23 (01), 21–32.
Mair, J.L., Goldfarb, R.J., et al., 2006. Geochemical Constraints on the Genesis of the Scheelite Dome Intrusion-Related Gold Deposit, Tombstone Gold Belt, Yukon. Canada. Economic Geology 101, 523–553.
Marsh, E.E., Goldfarb, R.J., et al., 2003. Geology and geochemistry of the Clear Creek intrusion-related gold occurrences, Tintina Gold Province, Yukon. Canada. Can. J. Earth Sci. 40, 681–699.
Newberry, R.J., McCoy, D.T., Brew, D.A., 1995. Plutonic-hosted gold ores in Alaska: Igneous vs. metmorphic origins. In: Ishihara, S., Czamanske, G.K. (Eds.), Proc. Sapporo International Conf. on Mineral Resources of the NW Pacific Rim, Res Geol, Spec Iss. vol. 18, pp. 57–100.
Niu, Y.L. and O'Hara, M.J. 2003. Origin of ocean island basalts: A new perspective from petrology, geochemistry, and mineral physics considerations. Journal of Geophysical Research 108 (B4), doi: 10. 1029/2002JB002048.
Ohmoto, H., 1986. Stable isotope geochemistry of ore deposits. Rev. Mineral. 16, 491–560.
Patten, C.G.C., Pitcairn, I.K., Molńar, F., Kolb, J., Beaudoin, G., Guilmette, C., Peillod, A., 2020. Gold mobilization during metamorphic devolatilization of Archean and Paleoproterozoic metavolcanic rocks. Geology 48, 1110–1114.
Qi, X.P., Yang, J., Fan, X.G., et al., 2016. Age, geochemical characteristics and tectonic significance of Changshishan ophiolite in central East Kunlun tectonic mélange belt along the east section of East Kunlun Mountains. Geology in China 43, 797–816 in Chinese with English abs.
Robinson, B.W., Kusakabe, M., 1975. Quantitative preparation of SO2 for 34S/32S analyses from sulphides by combustion with cuprous oxide. Anal. Chem. 47, 1179–1181.

Roedder, E., 1984. Fluid Inclusions. Mineralogical Society of America, Virginia.
Ren, J.H., Liu, Y.Q., et al., 2009. LA-ICP-MS U-Pb zircon dating and geochemical characteristics of diabase-dykes from the Qingshuiquan area, eastern Kunlun orogenic belt. Acta Petrologica Sinica 25 (5), 1135–1145.
Rogers, A.J., Kolb, J., Meyer, F.M., Vennemann, T., 2013. Two stages of gold mineralization at Hutti mine. India Miner. Deposita 48, 99–114.
Rollinson, H.R., 1993. Using Geochemical Data: Evalution, Presentation Interpretation. Longman Scientific and Technical Press 306–308.
Reich, M., Kesler, S.E., Utsunomiya, S., et al., 2005. Solubility of gold in arsenian pyrite. Geochem. Cosmochim. Acta 69, 2781–2796.
Reich, M., Deditius, A., et al., 2013. Pyrite as a record of hydrothermal fluid evolution in a porphyry copper system: a SIMS/EMPA trace element study. Geochem. Cosmochim. Acta 104, 42–62.
Sui, J., Li, J., Wen, G., Jin, X., 2017. The Dewulu reduced Au-Cu skarn deposit in the Xiahe-Hezuo district, West Qinling orogen, China: implications for an intrusion-related gold system. Ore Geol. Rev. 80, 1230–1244.
Sun, F.Y., Li, B.L., Ding, Q.F., et al., 2009. Research on the Key Problems of Ore Prospecting in the Eastern Kunlun Metallogenic Belt. Geological Survey Institute of Jilin University, Changchun (in Chinese).
Sillitoe, R.H., Thompson, J., 1998. Intrusion-related vein gold deposits: Types, tectono-magmatic settings and difficulties of distinction from orogenic gold deposits. Resour. Geol. 48, 237–250.
Sillitoe, R.H., 1991. Gold metallogeny of Chile an introduction. Econ. Geol. 86, 1187–1205.
Saravanan, C.S., Mishra, B., 2009. Uniformity in sulfur isotope composition in the orogenic gold deposits from the Dharwar Craton, southern India. Miner. Deposita 44, 597–605.
Tao, J.J., 2014. Characteristics of fluid inclusions and genesis of Annage gold deposit, Qinghai Province. Zhong'nan University (in Chinese with English abstract). Master's dissertation of.
Taylor, S.R., McLennan, S.M., 1985. The Continental Crust: Its Composition and Evolution. Blackwell Scientific Publications, Oxford, p. 312.
Thompson, J., Newberry, R.J., 2000. Gold deposits related to reduced granitic intrusions. In: Hagemann, S.G., Brown, p.e. (Eds.), Gold in 2000Reviews in Econ. Geol. vol. 13. Society of Economic Geologists, Inc., Denver, pp. 377–400.
Vikent'eva, O.V., Prokofiev Vsevolod, Y.u., 2018. Intrusion-related gold-bismuth deposits of North-East Russia: PTX parameters and sources of hydrothermal fluids. Ore Geol. Rev. 102 (2018), 240–259.
Wang, G.C., Wei, Q.R., et al., 2007. Some ideas of Precambrian geology in the East Kunlun. China. Geol. Bull. China 26, 929–937 in Chinese with English abs.
Wei, B., 2015. Study on the geological characteristic and tectonic attribute of the ophiolite and island-arc-type igneous rocks, Central belt of East Kunlun (Eastern Section). of Chang'an University (in Chinese with English abstract). Master's dissertation.
Wang, C., Liu, L., Xiao, P.X., Cao, Y.T., Yu, H.Y., Meert, J.G., Liang, W.T., 2014. Geochemical and geochronologic constraints for Paleozoic magmatism related to the orogenic collapse in the Qimantagh-South Altyn region, northwestern China. Lithos 202–203, 1–20.
Wang, X.X., Hu, N.G., Wang, T., et al., 2012. Late Ordovician Wanbaogou granitoid pluton from the southern margin of the Qaidam basin: Zircon SHRIMP U-Pb age, Hf isotope and geochemistry. Acta Petrol. Sin. 28 (9), 2950–2962.
Xiong, F., Ma, C., Wu, L., et al., 2015. Geochemistry, zircon U-Pb ages and Sr–Nd–Hf isotopes of an Ordovician appinitic pluton in the East Kunlun orogen: New evidence for Proto-Tethyan subduction. J. Asian Earth Sci. 111, 681–697.
Xiong, L.J., 2014. Tectonic Evolution and Processes in the West Segment of the Northern Proto-Tethys Tectonic Domain. Ocean University of China, Qingdao. Master thesis.
Xiong, F.H., Ma, C.Q., Zhang, J.Y., et al., 2014. Reworking of old continental lithosphere: an important crustal evolution mechanism in orogenic belts, as evidenced by Triassic I-type granitoids in the East Kunlun orogen, Northern Tibetan Plateau. J. Geol. Soc. London 171 (6), 847–863.
Xiao, Y., Feng, C.Y., Li, D.X., Liu, J.N., 2014. Chronology and fluid inclusions of the Guoluolongwa gold deposit in Qinghai province. Acta Geologica Sinica 88, 895–902 in Chinese with English abs.
Yang, J.S., Robinson, P.T., Jiang, C.F., Xu, Z.Q., 1996. Ophiolites of the Kunlun Mountains, China and their tectonic implications. Tectonophysics 258, 215–231.
Yuan, H.L., Gao, S., Liu, X.M., et al., 2004. Accurate U-Pb age and trace element determinations of zircon by laser ablation inductively coupled plasma mass spectrometry. Geostandard Newslett. 28, 353–370.
Zhang, Y.T., Sun, F.Y., 2018. Metallogenesis of gold deposits in Wulongou ore concentration Area, central segment of the east Kunlun Mountains, Qinghai province. Jilin University, China. Ph.D thesis.
Zhang, J.Y., Ma, C.Q., et al., 2017. A possible genetic relationship between orogenic gold mineralization and post-collisional magmatism in the eastern Kunlun Orogen, western China. Ore Geol. Rev. 81 (2017), 342–357.
Zhang, J.Y., Ma, C.Q., Xiong, F.H., Liu, B., Li, J.W., Pan, Y.M., 2014a. Early Paleozoic high-Mg diorite-granodiorite in the eastern Kunlun Orogen, western China: response to continental collision and slab break-off. Lithos 210, 129–146.
Zhang, C., Liu, Y., et al., 2014b. Characteristics of sulfur isotope geochemistry of the Xincheng gold deposit, Northwest Jiaodong. China. Acta Petrologica Sinica 30 (9), 2495–2506.
Zhang, Y.L., Hu, D.G., Shi, Y.R., Lu, L., 2010. SHRIMP zircon U-Pb ages and tectonic significance of Maoniushan Formation volcanic rocks in East Kunlun orogenic belt. China. Geol. Bull. China 29, 1614–1618 in Chinese with English abs.
Zhao, C.S., Yang, F.Q., et al., 2006. Metallogenic age of the Kendekeke Co, Bi, Au deposit in East Kunlun Mountains, Qinghai Province, and its significance. Mineral Deposits 25, 427–430 in Chinese with English abs.
Zhao, C.S., 2004. Gold, silver metallogeny in Eastern Kunlun Orogenic Belt, Qinghai Province: Ph.D. thesis. Jilin University, Changchun 144p (in Chinese with English abs.).
Zheng, Z., Chen, Y.J., Deng, X.H., et al., 2018. Origin of the Bashierxi monzogranite, Qiman Tagh, East Kunlun Orogen, NW China: A magmatic response to the evolution of the Proto-Tethys Ocean. Lithos 296–299, 181–194.
Zheng, Y.F., Chen, J.F., 2000. Stable isotope geochemistry. Science Press, Beijing, pp. 218–239.
Zhu, Y.H., Pan, Y.M., Zhang, K.X., Chen, N.S., Wang, G.C., Hou, G.J., 2000. Mineralogical characteristics and petrogenesis of ophiolites in East Kunlun Orogenic Belt. Qinghai Province. Acta Miner. Sin. 20, 128–142 in Chinese with English abs.
Zhu, B.Q., Li, X.H., et al., 1998. Isotopic system theory and application to the earth science: On crust-mantle evolution of continent of China [M]. Science Press, Beijing, pp. 216–226.
Zartman, R.E., Doe, B.R., 1981. Plumbotectonics-the model. Tectonophysics 75, 135–162.
Zhou, B., Dong, Y.P., et al., 2016. Geochemistry and zircon U-Pb geochronology of granitoids in the East Kunlun Orogenic Belt, northern Tibetan Plateau: origin and tectonic implications. J. Asian Earth Sci. 130 (2016), 265–281.